



# Evolution of soil-water states in the vadose zone of a desert soil after an extreme rainfall event and its impact on the ecosystem

Hong Zhou<sup>1,2</sup> · Wen Zhi Zhao<sup>2</sup>

Received: 29 October 2020 / Accepted: 26 May 2021 / Published online: 15 June 2021  
© Springer-Verlag GmbH Germany, part of Springer Nature 2021

## Abstract

Evolution of soil-water movement patterns following rare and extreme rainfall events in arid climates is not well understood, but it has significant effects on water availability for desert plants and on the hydrological cycle at small scale. Here, field data and the Hydrus-1D model were used to simulate the mechanisms of soil water and vapor transport, and the control factors associated with temporal variability in the soil water and temperature were analyzed. The results showed that thermal vapor transport with a no rainfall scenario determined daily variability in water content at the soil surface. During rainfall, isothermal liquid water fluctuated as a result of dry sandy soils and matric potential in the upper soil (0–25 cm), and thermally driven vapor played a key role in soil-water transport at 40–60 cm soil depth. After an extreme rainfall event, thermal vapor flux increased and accounted for 11.8% of total liquid and vapor fluxes in daytime with a steep temperature gradient; this was very effective in improving long-term soil-water content after the rain. The simulated results revealed that thermal water vapor greatly contributed to the soil-water balance in the vadose zone of desert soil. This study provided an alternative approach to describing soil-water movement processes in arid environments, and it increased understanding of the availability of water for a desert plant community.

**Keywords** Unsaturated zone · Liquid water and water vapor movement · Rainfall · Desert system · Hydrus-1D

## Introduction

Understanding the evolution processes of water states and water movement patterns in the vadose zone of soils is central to quantifying water resources in dry environments (Saito et al. 2006; Scanlon et al. 2003). Soil water, especially near the soil surface, is the key control variable in the groundwater-soil-plant-atmosphere continuum (Noy-Meir 1973), and it is influenced by evaporation, precipitation, and vadose zone properties. In most cases, soil-water transport occurs in the liquid phase; however, in arid ecosystems, where rainfall is scarce and highly intermittent, soil moisture approaches residual water content, reducing soil hydraulic conductivity and

increasing vapor content; this is accompanied by soil thermal gradients which may induce water fluxes in vapor and liquid phases (Deb et al. 2011). In particular, movement of vapor becomes a major component of water transfer in dry soils.

It has been widely recognized that the movement of water and heat in soils is coupled and they strongly affect each other (Bouyoucos 1915). Prior research on isothermal liquid water movement was based on the Richards equation, extended to the movement of liquid and vapor with the Penman equation (Penman 1940; Philip 1957; Philip and Vries 1957; Richards and Richards 1931). Following modifications (Bristow and Horton 1996; Cass et al. 1984; Milly 1982, 1984, 1996; Nassar and Horton 1997; Webb and Ho 1998), the theory of coupled liquid water-vapor-heat transport in the unsaturated zone was proposed, and became known as the PDV model (Philip and Vries 1957). In the model, the total soil-water flux includes four components: thermal liquid, thermal vapor, isothermal liquid and isothermal vapor fluxes. Furthermore, soil water represented by water vapor adsorption of nonrainfall water is an important component of the soil-water budget and energy balance in unsaturated soils (Milly 1984, 1996; Parlange et al. 1998; Scanlon 1994; Uclés et al. 2016). In particular, thermally driven flow of water vapor is an

✉ Wen Zhi Zhao  
zhaowzh@lzb.ac.cn

<sup>1</sup> College of Tourism, Northwest Normal University,  
Lanzhou 730070, China

<sup>2</sup> Northwest Institute of Eco-Environment and Resources, Chinese  
Academy of Sciences, Linze Inland River Basin Research Station,  
Key Laboratory of Inland River Basin Ecohydrology,  
Lanzhou 730000, China

important water cycle process that can affect water movement in arid climates as a result of dry soils and steep temperature gradients (Andraski et al. 2005; Saito et al. 2006); such flow is responsible for dew formation, among others (Uclés et al. 2015, 2016; Zhuang and Zhao 2017).

Based on these theoretical models and field research, various experimental and numerical studies were conducted to better understand water movement in both liquid and vapor phases, and heat transfer in the vadose zone. Several studies evaluated coupled water fluxes and their temporal variability in the vadose zone in controlled experiments (Sakai et al. 2009; Zeng et al. 2011; Zeng et al. 2009). Other studies addressed the influence of vegetation, soil heat and texture, and rainfall on liquid water, water vapor, and heat transport using field experiments (Bittelli et al. 2008; Deb et al. 2011; Garcia et al. 2011; Huang et al. 2015; Madi and Rooij 2015; Wu et al. 2017). It is now generally accepted that vapor flow in soils is a valuable component of the hydrological cycle in extremely dry regions (Du et al. 2017).

Northwestern China is a semiarid and arid region with several large deserts, which span 53% of the land area. Deserts in the area include the Badain Jaran and Tengger. The Linze Inland River Basin Research Station is located at the southern edge of the Badain Jaran Desert. In this area, the most important geomorphologic feature is characterized by sand dunes, alternating with lightly undulating interdunal lowlands (Zhou et al. 2016). The total annual precipitation in this region is less than 110 mm, and rain constitutes the only possible water source for the vadose zone. In contrast to the low precipitation, the average annual pan evaporation is estimated to be 2,388 mm (Zhuang and Zhao 2017), or twenty times greater than the annual precipitation (Zhang et al. 2017). Furthermore, rainfall is dominated by small events which can completely evaporate before seeping into deep soil layers (Li et al. 2010). These conditions are indicative of an extremely arid continental climate with water-limited areas (Mcvicar et al. 2012); however, even in such an extremely dry environment, soil-water content at 10–40-cm depth exhibits noticeable fluctuations with daily temperature changes (Zhang et al. 2007; Zhang and Wei 2003). This indicates a presence of other, nonrainfall water sources supplying soil water in the deserts (Uclés et al. 2016). One such possible water source may be soil-water vapor adsorption (Ramírez et al. 2007); however, only a few studies have focused on the transport of liquid water, water vapor, and heat in the unsaturated zone, and evaluated relations between soil water and a rainfall event; in particular, understanding the contribution of vapor flux to total water flux is still limited under rainfall conditions in desert soils such as in the Badain Jaran desert.

In extreme deserts, only light rainfalls replenish moisture in shallow soil layers; therefore, water fluxes are often small and liquid water movement is normally suppressed in low soil moisture conditions (Knapp et al. 2008). Thus, the transfer

of vapor and its driving factors between the vadose zone and the atmosphere, and the vapor-driving factors, have an important impact on the soil-water balance. In addition, thermally driven vapor flow and condensation supplement soil water to plant roots during the driest periods in arid regions (Garcia et al. 2011). An evaluation of these processes requires a combination of adequate field measurements and numerical models (Scanlon 1994). Meanwhile, the potential for an increase in the intensity of extreme rainfall events with climate change is of significant societal concern (Westra et al. 2015).

In this study, an extreme rainfall event was selected during the period of highest ground temperature to monitor soil-water balance in a typically extremely dry soil. In addition, a coupled Hydrus-1D model was used to simulate continuous changes in water contents and temperatures. The aim of this study was to: (1) compare the driving factors of liquid water and vapor migration in soil in an extreme rainfall event, and in a rain-free period, (2) describe patterns of soil-water transport at different depths during three stages: before dawn, at daytime, and nighttime, and (3) investigate the possible relationships between plant root biomass and available soil water.

## A liquid water-vapor-heat coupling-migration-model theory

### Water flow module

The Hydrus-1D software package (version 4.15) was used to simulate the coupled liquid water-water vapor-and-heat transport; the governing equation for one-dimensional (1D) flow was calculated as follows:

$$\frac{\partial \theta}{\partial t} = \frac{\partial q_l}{\partial z} - \frac{\partial q_v}{\partial z} \quad (1)$$

$$\theta = \theta_l + \theta_v \quad (2)$$

where  $\theta$  is the soil total volumetric water content ( $\text{cm}^3 \text{cm}^{-3}$ ),  $q_l$  and  $q_v$  are flux densities of liquid water and water vapor ( $\text{cm h}^{-1}$ ), respectively,  $t$  is time (hour),  $z$  is the spatial coordinate positive upward (cm), and  $\theta_l$  and  $\theta_v$  were volumetric liquid water and water vapor contents ( $\text{cm}^{-3} \text{cm}^{-3}$ ), respectively.

The flux density of liquid water ( $q_l$ ) and water vapor ( $q_v$ ) are described using a modified version of Darcy's law (Philip and Vries 1957):

$$q_l = q_{lh} + q_{lT} = -K_{lh} \left( \frac{\partial h}{\partial z} + 1 \right) - K_{lT} \frac{\partial T}{\partial z} \quad (3)$$

$$q_v = q_{vh} + q_{vT} = -K_{vh} \frac{\partial h}{\partial z} - K_{vT} \frac{\partial T}{\partial z} \quad (4)$$

where  $q_{lh}$  and  $q_{lT}$  are isothermal and thermal liquid water flux

densities ( $\text{cm h}^{-1}$ ), and  $q_{\text{vh}}$  and  $q_{\text{vT}}$  are isothermal and thermal vapor water flux densities ( $\text{cm h}^{-1}$ ) respectively,  $h$  is the pressure head (cm),  $T$  is temperature ( $^{\circ}\text{C}$ ),  $K_{\text{lh}}$  ( $\text{cm h}^{-1}$ ) and  $K_{\text{lT}}$  ( $\text{cm}^2 \text{ }^{\circ}\text{C}^{-1} \text{ h}^{-1}$ ) are isothermal and thermal hydraulic conductivities for liquid phase fluxes, and  $K_{\text{vh}}$  ( $\text{cm h}^{-1}$ ) and  $K_{\text{vT}}$  ( $\text{cm}^2 \text{ }^{\circ}\text{C}^{-1} \text{ h}^{-1}$ ) are isothermal and thermal hydraulic conductivities for vapor fluxes, respectively. Therefore, combining Eqs. (1), (2), and (3), the water balance equation for vadose zone soil becomes:

$$\frac{\partial \theta}{\partial t} = \frac{\partial}{\partial Z} \left[ K_{\text{lh}} \frac{\partial h}{\partial Z} + K_{\text{lh}} + K_{\text{lT}} \frac{\partial T}{\partial Z} + K_{\text{vh}} \frac{\partial h}{\partial Z} + K_{\text{vT}} \frac{\partial T}{\partial Z} \right] \quad (5)$$

$$K_{\text{Th}} = K_{\text{lh}} + K_{\text{vh}} \quad (6)$$

$$K_{\text{TT}} = K_{\text{lT}} + K_{\text{vT}} \quad (7)$$

where  $K_{\text{Th}}$  ( $\text{cm h}^{-1}$ ) and  $K_{\text{TT}}$  ( $\text{cm}^2 \text{ }^{\circ}\text{C}^{-1} \text{ h}^{-1}$ ) are isothermal and thermal total hydraulic conductivities, respectively. The detailed methods for these parameters were taken from the work of Du et al. (2017).

### Soil hydraulic properties

The soil hydraulic properties were modeled using the Van Genuchten-Mualem model (VG model) (Genuchten 1980; Mualem and Yechezkel 1976).

$$\theta(h) = \begin{cases} \theta_r + \frac{\theta_s - \theta_r}{[1 + |\alpha h|^n]^m}, & h < 0 \\ \theta_s, & h \geq 0 \end{cases} \quad (8)$$

$$m = 1 - 1/n, n > 1$$

$$k(h) = K_s S_e^l \left[ 1 - \left( 1 - S_e^{1/m} \right)^m \right]^2 \quad (9)$$

$$S_e = \frac{\theta(h) - \theta_r}{\theta_s - \theta_r}$$

where  $S_e$  is the effective saturation ( $\text{cm}^{-3} \text{ cm}^{-3}$ ),  $\theta_s$  and  $\theta_r$  are the saturated water content and residual water content ( $\text{cm}^{-3} \text{ cm}^{-3}$ ), respectively,  $K_s$  is the soil saturated hydraulic conductivity ( $\text{cm h}^{-1}$ ),  $\alpha$  is an air entry parameter ( $^{-1}$ ),  $n$  is a pore-size distribution parameter, and  $l$  is a pore connectivity parameter.

### Heat transport module

The governing conservation equation for heat movement in soil is given by the following (Nassar et al. 1992):

$$\begin{aligned} \frac{\partial C_p T}{\partial t} + L_0 \frac{\partial \theta_v}{\partial t} \\ = \frac{\partial}{\partial Z} \left[ \lambda(\theta) \frac{\partial T}{\partial Z} \right] - C_w \frac{\partial q_L T}{\partial Z} - L_0 \frac{\partial q_v}{\partial Z} - C_v \frac{\partial q_v T}{\partial Z} \end{aligned} \quad (10)$$

where  $\lambda(\theta)$  is the apparent thermal conductivity ( $\text{J cm}^{-1} \text{ h}^{-1} \text{ }^{\circ}\text{C}^{-1}$ );  $C_p$ ,  $C_w$ , and  $C_v$  are volumetric heat capacities ( $\text{J cm}^{-3} \text{ }^{\circ}\text{C}^{-1}$ ) of the soil, liquid phase, and vapor phase, respectively; and  $L_0$  is the volumetric latent heat of vaporization of liquid water ( $\text{J cm}^{-3}$ ).

### Soil heat properties

The apparent thermal conductivity in the absence of flow and macrodispersivity may be expressed as follows (Chung and Horton 1987; Marsily 1986):

$$\lambda(\theta) = \lambda_0(\theta) + \beta_t C_w |q| \quad (11)$$

$$\lambda_0(\theta) = b_1 + b_2 \theta + b_3 \theta^{0.5} \quad (12)$$

where  $\beta_t$  is the thermal dispersivity (cm);  $q$  is the water flux;  $b_1$ ,  $b_2$  and  $b_3$  are empirical parameters ( $\text{W cm}^{-1} \text{ }^{\circ}\text{C}^{-1}$ ); all implemented in Hydrus-1D code.

### Initial and boundary conditions

#### Initial conditions

Initial conditions included variable temperature and pressure head in soil layers; pressure head was determined from the VG model. Here, the corresponding initial pressure head ( $h$ ) was calculated from the water retention curve based on the initial volumetric water content. Initial soil temperature ( $T$ ) values for each node were interpolated using measured data.

#### Boundary conditions

The upper boundary for water flux was used for the time-variable atmospheric boundary condition including potential evaporation, air temperature, and rainfall; input values were based on daily data of air temperature, solar radiation sun hours and rainfall. The lower water flow boundary was free drainage due to absence of groundwater; and the lower boundary condition for heat transport was specified as zero-temperature gradient. Because the water table was deep ( $>4$  m), heat transfer across the lower boundary was assumed to occur only by convection of liquid water and water vapor phase. In addition, the soil profile was considered to be 100 cm in depth, and it was discretized into finite elements of 1 cm, leading to 101 nodes across the water flow domain. Field data were obtained for a period of 153 days from May 1 to September 30 in 2017 and 2018, respectively.

### Accuracy of modeling results

The quality of model performance was evaluated with root-mean squared error (RMSE) and  $R^2$ ; this has been commonly used to assess the simulation power of hydrological discharge

models (Willmott 1981).

$$\text{RMSE} = \sqrt{\frac{1}{n} \sum_{i=1}^n (S_i - O_i)^2} \quad (13)$$

$$R^2 = \frac{\left[ \sum_{i=1}^n (O_i - \bar{O})(S_i - \bar{S}) \right]^2}{\left[ \sum_{i=1}^n (O_i - \bar{O})^2 \sum_{i=1}^n (S_i - \bar{S})^2 \right]} \quad (14)$$

where  $n$  is the number of paired observations,  $O_i$  and  $S_i$  are the observed and simulated values, respectively,  $\bar{O}$  and  $\bar{S}$  are the mean of the observed and simulated values, respectively.

## Materials and methods

### Study site

The study area is located in the arid region of northwestern China, in the middle part of the Heihe River basin, which has a drainage area of  $1.3 \times 10^5 \text{ km}^2$  (Zhao et al. 2011). The experiment was carried out near the Linze Inland River Basin Research Station, Chinese Academy of Sciences (latitude  $39^\circ 21' \text{N}$ , longitude  $100^\circ 07' \text{E}$ , at an elevation of 1,374 m above mean sea level), located at the southern edge of the Badain Jaran Desert, and the experimental field was located on a sand dune (Fig. 1). The climate at this location can be described as temperate continental, with cool winters and hot summers. Based on meteorological data collected at the station in years 1965–2017, the area receives 117 mm of rainfall annually, of which 65% falls from July to September. Average annual potential evaporation is estimated to be 2,388 mm, and the annual duration of sunlight totals 3,045 h. Average annual temperature for the experimental site is  $7.6^\circ \text{C}$ , with the maximum of  $39^\circ \text{C}$  in July, and minimum of  $-27^\circ \text{C}$  in January. Relative humidity fluctuates throughout the year from 7.3 to 80.9% (Zhao and Zhao 2014), and the annual average wind speed is about 3.2 m/s. The site was characterized by sand-stabilized dunes alternating with lightly undulating interdune lowlands (Zhou et al. 2016). Natural vegetation is mainly sparse desert shrub, including *Haloxylon ammodendron*, and *Nitraria sphaerocarpa*. The soil is comprised mainly of fine to coarse sand fractions, with only 0.1–1.73% clay (Table 1).

### Measurements

#### Soil-water retention curve

Soil-water retention curves were measured in the laboratory using a high-speed centrifuge (H1400 PF, JAPAN, KOKUSAN), and modeled using the RETC code (Fig. 2), and its corresponding VG parameters are listed in Table 2.

### Meteorological data

Hourly data for rainfall amount, maximum and minimum air temperature, relative humidity, and average daily wind speed, and daily duration of bright sunshine, were collected by the Linze Inland River Basin Research Station personnel, Chinese Academy of Sciences, near the experimental field from 1 May to 30 September of 2017 and 2018 (Fig. 3).

### Soil-water content and temperature

For the initial experiment, soil-water sensors (5TM, Decagon, USA) were installed at six different depths: 5, 15, 25, 40, 60, and 100 cm below ground surface, along the wall of an excavated pit. The sensors were inserted into horizontally drilled guide-holes. Soil water was monitored throughout the study period using data loggers (EM50, METER Group, USA) with a frequency of every 1 min. Meanwhile, soil temperature was measured automatically over the 0–100 cm depth at 1-min intervals using these sensors.

### Pressure head

At the experimental site, sandy soil has very low water content and the matric potential was difficult to capture directly by the monitoring equipment. Thus, soil water was first measured, and then transformed into the matric potential using the VG model (Du et al. 2017).

### Water-table depth

Water-table depth was measured daily with mini-diver sensor devices (Hobo, USA). The results showed that the water-table depth fluctuated in the range from 3.7 to 4.8 m in 2017 (Fig. 4). Changes in the water table can be divided into three periods during any one year, determined by groundwater use and agricultural irrigation (Yao et al. 2018a, b).

### Plant root investigation

Trenching was used to investigate root biomass and distribution in this study. A total of six trenches were made, including two trenches per quadrat and three quadrats per plot. Soil samples were collected from each soil layer at 10-cm intervals to 1-m depth in each trench. These samples were then stored in paper bags until oven-drying at  $80^\circ \text{C}$  for 24 h to a constant weight.

### Rainfall events

During 2003 to 2017 in the study area, a total of 501 rainfall events were detected at meteorological stations (Fig. 5). An extreme rainfall event occurred on 21 July 2017, with rainfall

**Table 1** Soil texture, saturated hydraulic conductivity and bulk density from the stabilized dunes

| Soil depth (cm) | Soil particle content (%) |      |       | FC<br>(cm <sup>3</sup> cm <sup>-3</sup> ) | K <sub>S</sub><br>(cm h <sup>-1</sup> ) | BD<br>(g cm <sup>-3</sup> ) | SP<br>(%) | Soil texture |
|-----------------|---------------------------|------|-------|---|---|-----------------------------|-----------|--------------|
|                 | Clay                      | Silt | Sand  |   |   |                             |           |              |
| 5               | 1.73                      | 10   | 88.26 | 0.3                                       | 50.85                                   | 1.35                        | 45.28     | Sandy        |
| 15              | 1.41                      | 6.6  | 92.00 | 0.31                                      | 138.4                                   | 1.41                        | 46.42     | Sandy        |
| 25              | 1.28                      | 7.0  | 91.73 | 0.37                                      | 140.28                                  | 1.45                        | 46.42     | Sandy        |
| 40              | 1.55                      | 6.76 | 91.7  | 0.29                                      | 140.54                                  | 1.50                        | 46.79     | Sandy        |
| 60              | 1.28                      | 6.14 | 92.58 | 0.25                                      | 116.76                                  | 1.44                        | 46.04     | Sandy        |
| 100             | 0.01                      | 2.17 | 97.83 | 0.36                                      | 156.22                                  | 1.54                        | 38.11     | Sandy        |

Note: *FC* field water capacity; *K<sub>S</sub>* saturated hydraulic conductivity; *BD* bulk density; *SP* soil porosity

duration of 11 h and maximum rain intensity of 3.2 mm h<sup>-1</sup>. This rainfall event was selected for the simulation of movement of liquid water and vapor in the vadose zone of desert

soil. Daily rainfall categories based on previous reports (classifications 1, 2) and proposed in this work (classification 3) are given in Table 3 (Aronica et al. 2002, 2013), and the

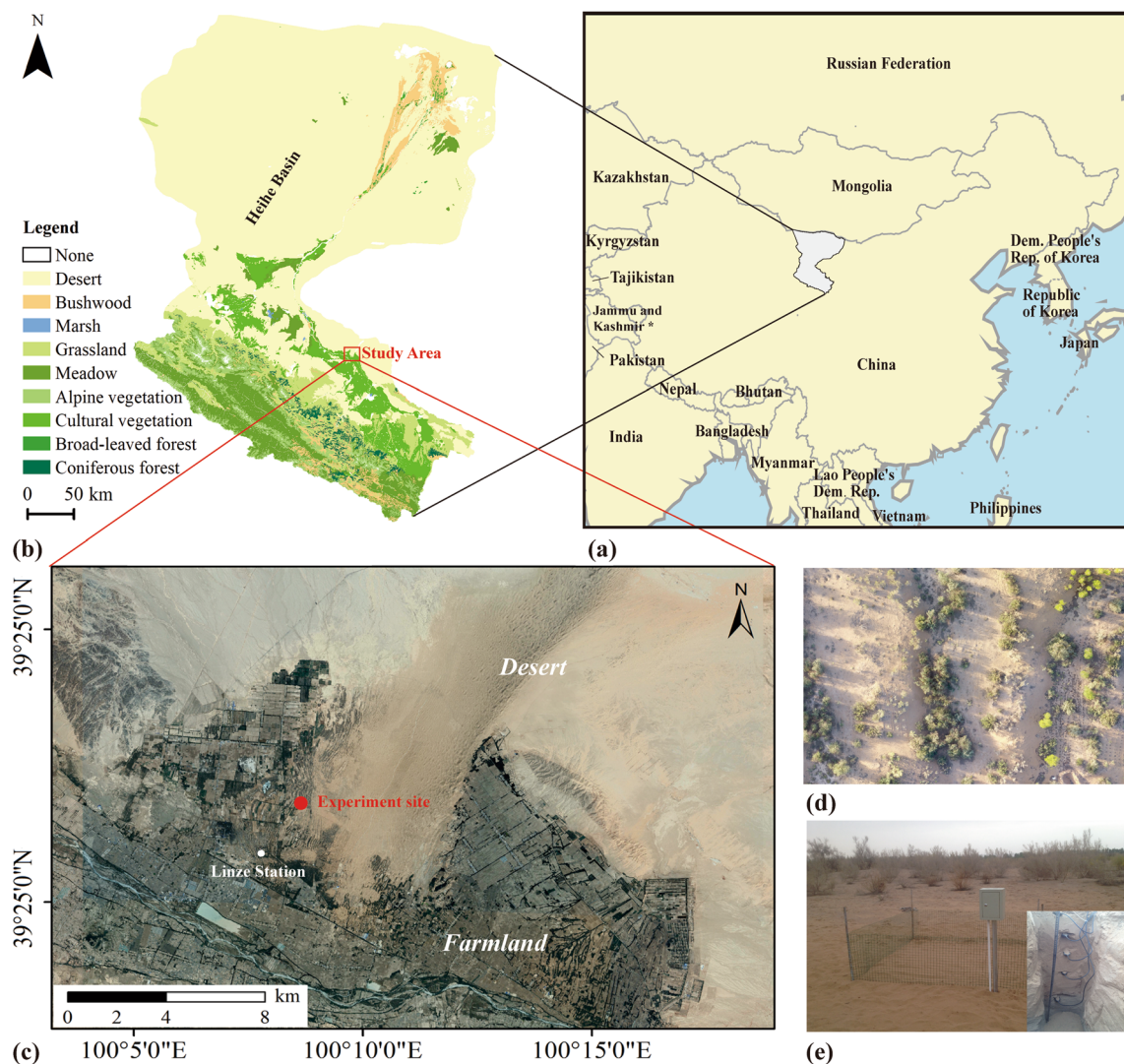


**Fig. 1** a Location of the study area, b Heihe River Basin and its vegetation types and location in China, c experimental site, d sand dune landscape, e observational instruments of the desert vadose zone.

(Borders and country/region names shown are based on the United Nations world map (UN 2021); \*The final status of Jammu and Kashmir has not been agreed upon by the parties)

**Table 2** The VG model parameters based on RETC model

| Soil depth (cm) | $\theta_s$ ( $\text{cm}^3 \text{cm}^{-3}$ ) | $\theta_r$ ( $\text{cm}^3 \text{cm}^{-3}$ ) | $n$ (–) | $a$ ( $\text{cm}^{-1}$ ) | $l$ |
|-----------------|---|---|---------|--------------------------|-----|
| 5               | 0.37  | 0.08  | 2.14    | 0.017                    | 0.5 |
| 15              | 0.37  | 0.06  | 2.29    | 0.012                    | 0.5 |
| 25              | 0.37  | 0.07  | 2.6     | 0.014                    | 0.5 |
| 40              | 0.35  | 0.06  | 2.47    | 0.012                    | 0.5 |
| 60              | 0.36  | 0.05  | 2.3     | 0.013                    | 0.5 |
| 100             | 0.37  | 0.08  | 2.14    | 0.016                    | 0.5 |

characteristics of this rainfall event are given in Table 4. To understand how the movement of liquid water and vapor changed during the rain-free period—2 days before (18 July) and 2 days after (24 July) the rain—were added to the analysis.

## Results

### Calibration of the Hydrus-1D model

The results of the Hydrus-1D model simulations were in poor agreement with field measurement of the VG parameters. Therefore, the observed values of the soil-water content and soil temperature at soil depths of 5, 15, 25, 40, 60, and 100 cm for the 2017 season were used to optimize these parameters using the inverse model. Table 5 lists the calibrated parameter sets for different soil depths. The Hydrus-1D model was used

with the calibrated parameters to capture temporal soil-water dynamics, with an average  $R^2 = 0.8$  and  $\text{RMSE} = 0.006 \text{ cm}^3 \text{ cm}^{-3}$ , for all depths except for the top of the soil profile (i.e. 5–15 cm) where calibrations exhibited  $R^2$  of 0.72–0.78 and  $\text{RMSE}$  of 0.009–0.011  $\text{cm}^3 \text{ cm}^{-3}$ . The model predicted sharp increases in soil water due to a heavy rainfall event (Fig. 6a), and this was in agreement with the previous studies which showed Hydrus-1D was better at modeling rapidly fluctuating surface soil moisture driven by rainfall than at modeling the slowly fluctuating soil moisture (Chen et al. 2014). The simulated and measured temperatures during the calibration periods (Fig. 6b), and the heat parameter values obtained from the inverse model (Table 5) showed a strong agreement between the observed and predicted values with an average  $R^2 = 0.92$ , and  $\text{RMSE} = 1.22 \text{ }^\circ\text{C}$ .

### Validation of the Hydrus-1D model

The soil-water content and soil temperature at 5, 15, 25, 40, 60, and 100 cm soil depths observed during the 2018 study period were used to validate the model. The simulated and measured soil water and temperature during the validation periods are presented in Fig. 7a,b. The temporal soil-water dynamics were captured well with  $R^2 = 0.81$  and  $\text{RMSE} = 0.006 \text{ cm}^3 \text{ cm}^{-3}$ . Soil temperature exhibited a strong match between the observed and simulated values, with  $R^2 = 0.92$  and  $\text{RMSE} = 1.22 \text{ }^\circ\text{C}$ ; however, the Hydrus-1D model systematically predicted higher soil temperatures at 5 cm depth than actually measured values. This phenomenon could be explained by heat flux primarily affecting the temperature, since there was higher net radiation in 2018. Further, the differences could be

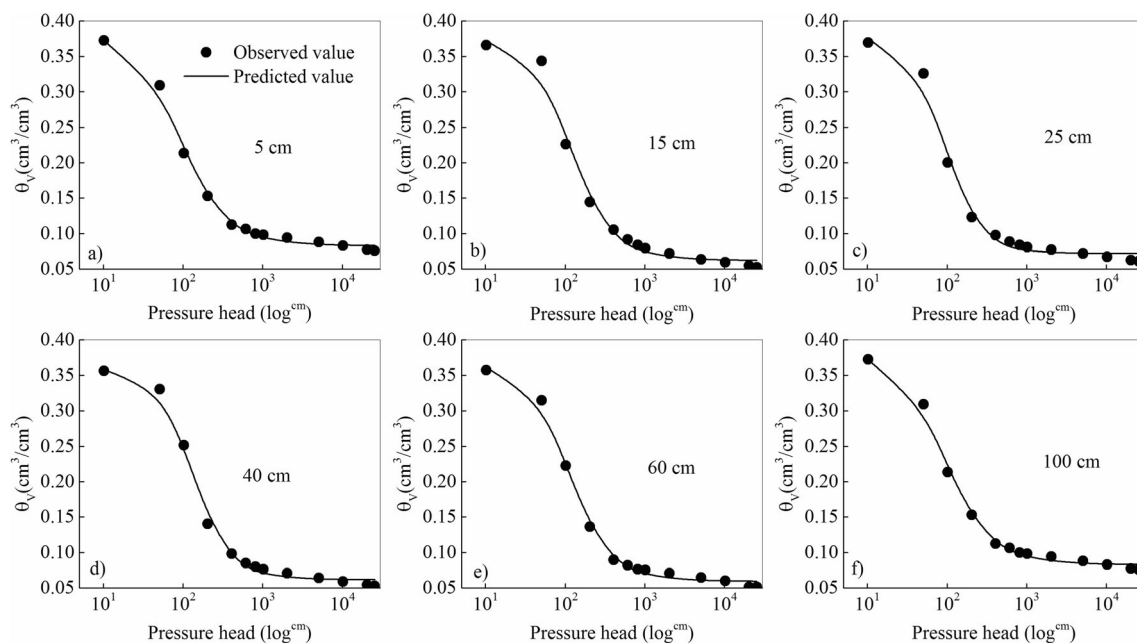


**Fig. 2** Soil-water retention curves at different soil depths in the study site

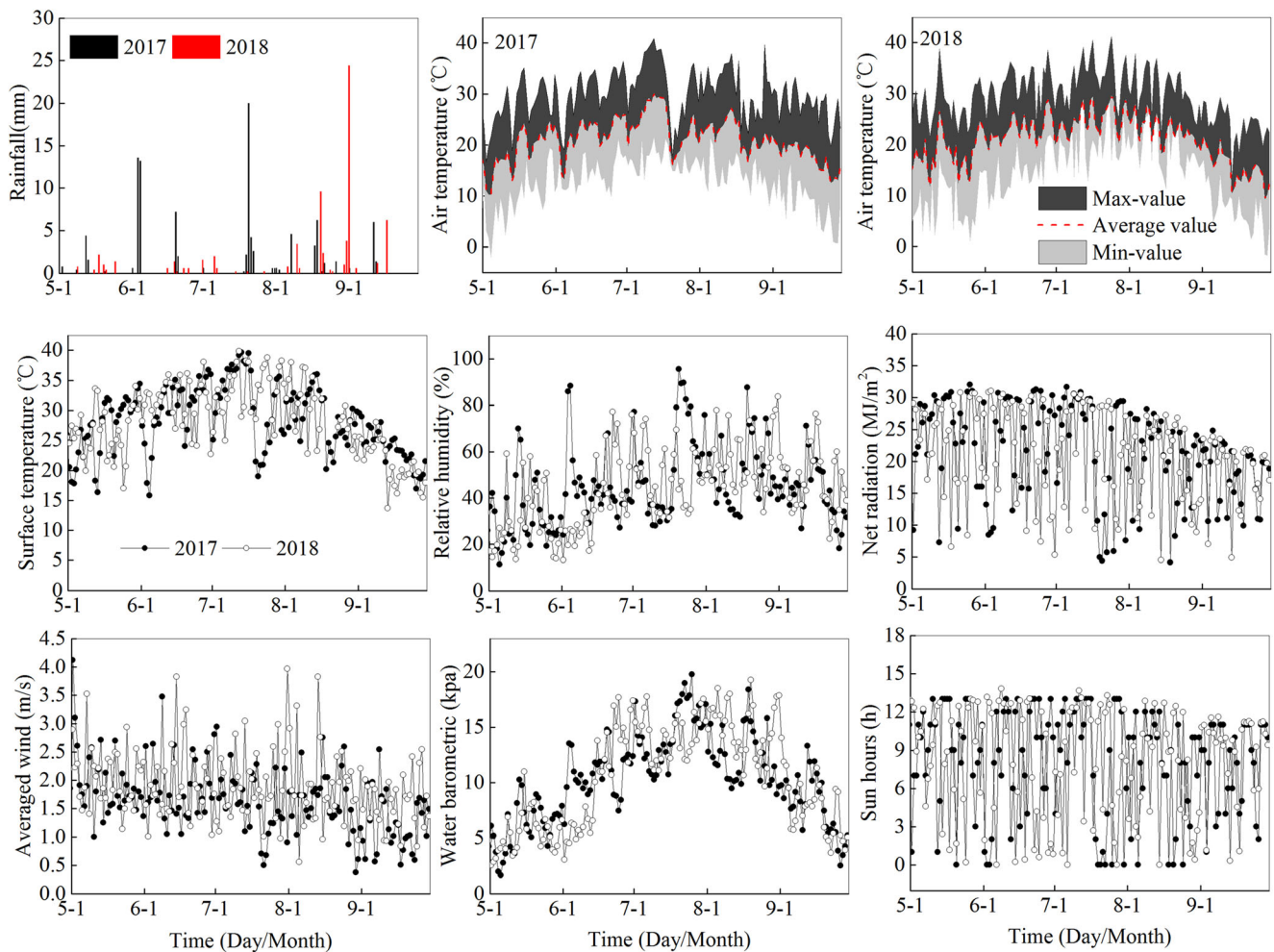


**Fig. 3** Daily dynamics of meteorological variables during the study period in 2017 and 2018

partially attributed to the errors associated with parameter optimization; these parameters could not truly reflect the soil properties and water flow behaviors due to the rough or incomplete soil classification system. Moreover, the simulation slightly overestimated the temperature at depths 40 and 60 cm (Fig. 7a), possibly due to vapor

transport in deeper soil, and it was found that from 20–100 days, evaporation is dominated by the vapor transport in conditions when almost no rainfall occurred. Overall, the correspondence between the observed and simulated soil-water content and temperature data during this validation period was satisfactory.

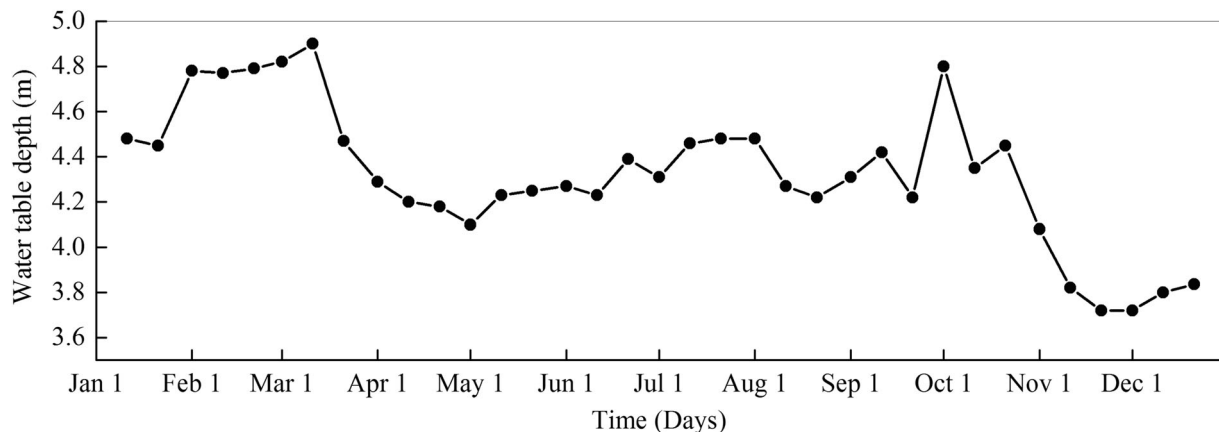


**Fig. 4** Daily dynamics of the water table in 2017 at the experimental site

**Table 3** Daily rainfall categories according to previous reports and proposed in this work (classification 3)

| Class | Classification 1                             |                  | Classification 2                     |                  | Classification 3                     |             |
|-------|--|------------------|--------------------------------------|------------------|--------------------------------------|-------------|
|       | Intensity ( $I$ )<br>(mm day <sup>-1</sup> ) | Description      | Intensity<br>(mm day <sup>-1</sup> ) | Description      | Intensity<br>(mm day <sup>-1</sup> ) | Description |
| 1     | $0.1 \leq I < 4$                             | Light            | $0.1 \leq I < 4$                     | Light            | $0.2 \leq I < 10$                    | Normal      |
| 2     | $4 \leq I < 6$                               | Light–moderate   | $4 \leq I < 20$                      | Moderate         | $10 \leq I < 20$                     | Heavy       |
| 3     | $16 \leq I < 32$                             | Moderate–heavy   | $I \geq 20$                          | Heavy–torrential | $I \geq 20$                          | Extreme     |
| 4     | $32 \leq I < 64$                             | Heavy            |                                      |                  |                                      |             |
| 5     | $64 \leq I < 128$                            | Heavy–torrential |                                      |                  |                                      |             |
| 6     | $I \geq 128$                                 | Torrential       |                                      |                  |                                      |             |

## Driving forces of liquid water and vapor

### Soil matric potential and its gradient

Figure 8a shows the daily dynamics of soil matric potential and its gradient during the simulated period (18–24 July 2017). Here, soil matric potential gradient  $\nabla h = h_{n+1} - h_n$ , whereby  $h_n$  is soil matric potential at depth  $n$ . During the study period, the matric potential fluctuated from  $-8,800$  to  $-140$  cm in the soil profile from 5 to 100 cm depth. The density of the contours changed from dense to sparse, then back to dense with increasing depth. Before the rain, changes in the soil matric potential occurred mainly in the top soil layers (0–10 cm); with the onset of rain and infiltration, the balance of soil matric potential was disrupted and pushed it down to depths between 20 and 30 cm. Instead, the contours of matric potential gradients were not depicted uniformly along the soil profile. Similarly, the contours near the surface were also the most intense, and the gradients were positive above the depth 60 cm and tended to be larger with increasing depth. However, with increasing rain amounts, the zero soil matric potential gradient planes did not appear, which is in agreement with earlier observations (Zeng et al. 2009).

### Soil temperature and its gradient

The daily time series of soil temperature is shown in Fig. 8b. Here, soil temperature gradient  $\nabla T = T_{n+1} - T_n$ , where  $T_n$  is

soil temperature at depth  $n$ . During the study period, soil temperatures varied from 17 to 39.8 °C in the soil profile from 0 to 100 cm. The isotherms near the surface (from 0 to 30 cm) indicated relatively fast changes in soil temperature along the profile, while the isotherms below 60-cm soil depth indicated little temperature variation with depth. However, these characteristics reversed from the rainfall event on 21 July. In addition, the variability in isotherms of the temperature gradient was similar to that for the soil temperature. The soil temperature gradient was positive at the depth of 0–100 cm before 21 July; after the rain on 21 July, the temperature gradient indicated a transition from positive to negative at the depth of 0–25 cm, with a maximum soil temperature change of 3 °C. Thus, the 0–25-cm soil depth layer was the most active layer for heat exchange. Temperature change decreased visibly with increasing soil depth, and the zero-gradient line occurred at 20 cm depth (Fig. 8b).

### Isothermal and thermal hydraulic conductivity

The isothermal and thermal hydraulic conductivity, including  $K_{lh}$  (cm h<sup>-1</sup>),  $K_{lT}$  (cm<sup>2</sup> °C<sup>-1</sup> h<sup>-1</sup>),  $K_{vh}$  (cm h<sup>-1</sup>), and  $K_{vT}$  (cm<sup>2</sup> °C<sup>-1</sup> h<sup>-1</sup>), were also important factors driving soil-water movement along the soil profile. The dynamics of  $K_{lh}$  (cm h<sup>-1</sup>),  $K_{lT}$  (cm<sup>2</sup> °C<sup>-1</sup> h<sup>-1</sup>),  $K_{vh}$  (cm h<sup>-1</sup>), and  $K_{vT}$  (cm<sup>2</sup> °C<sup>-1</sup> h<sup>-1</sup>) above 100-cm depth are shown in Fig. 8c, and indicate high variability in  $K_{lh}$  at 0–20 cm depth, rising

**Table 4** Characteristics of rainfall events during the study period: 18–24 July 2017

| Rainfall parameter   | Date (yyyy/m/dd) |           |             |            |             |            |           |
|----------------------|------------------|-----------|-------------|------------|-------------|------------|-----------|
|                      | 2017/7/18        | 2017/7/19 | 2017/7/20   | 2017/7/21  | 2017/7/22   | 2017/7/23  | 2017/7/24 |
| Rainfall amount (mm) | 0.0              | 0.2       | 2.2         | 20.6       | 4.2         | 2.6        | 0.0       |
| Time                 | 0                | 00:00     | 20:00–22:00 | 1:00–11:00 | 11:00–14:00 | 7:00–10:00 | 0         |
| Duration (hrs)       | 0                | 1         | 3           | 11         | 4           | 4          | 0         |
| Max amount per hour  | 0                | 0.4       | 1           | 3.2        | 2.2         | 0.8        | 0         |
| Rain phases          | Before           | During    | During      | During     | During      | During     | After     |



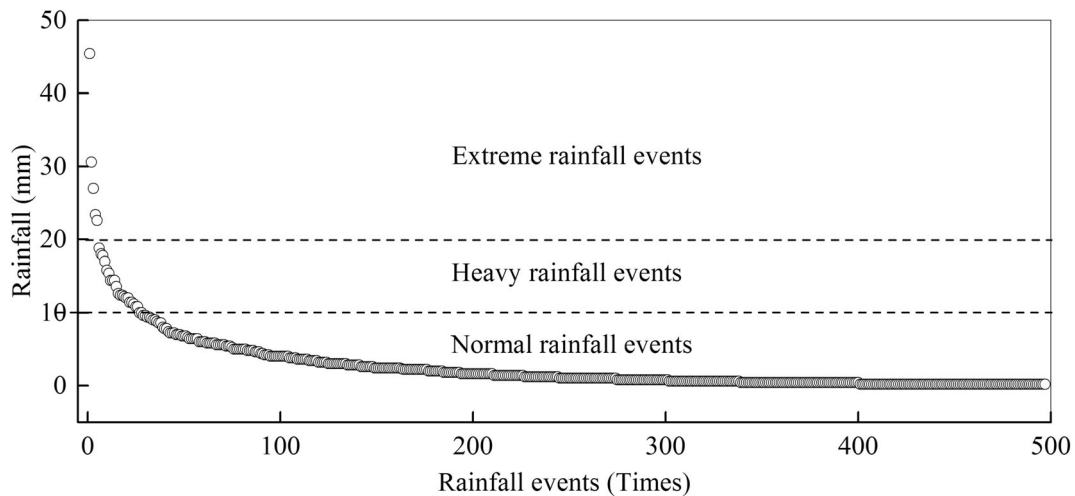


**Fig. 5** Classification of the past 15-year rainfall distribution in the study area

to  $0.07 \text{ cm h}^{-1}$  during the rainfall period. However, when infiltration stopped after the rainfall event, these values decreased as water moved downward through the soil; in particular, these values decreased even further during the drought period from 18 July to 21 July. The distribution of isolines of  $K_{IT}$  was similar to that of  $K_{lh}$  along the profile, but the value of  $K_{IT}$  was smaller than that of  $K_{lh}$ , ranging from  $2 \times 10^{-10}$  to  $0.04 \text{ cm}^2 \text{ }^\circ\text{C}^{-1} \text{ h}^{-1}$ .

The value of  $K_{vh}$  was very low during the study period and ranged from  $3 \times 10^{-8}$  to  $5 \times 10^{-11} \text{ cm h}^{-1}$ , especially during the rainfall events when  $K_{vh}$  was close to zero at depths between 0 and 30 cm. In addition, the value of  $K_{vT}$  was low during and after rainfall, but significantly higher than that of  $K_{vh}$ ; however, in conditions of a severe long-lasting drought,  $K_{vT}$  flux fluctuated greatly in the top soil at depths of approximately 0–10 cm. The maximum value at the soil surface reached  $0.013 \text{ cm}^2 \text{ }^\circ\text{C}^{-1} \text{ h}^{-1}$ .

**Dynamics of liquid water and vapor fluxes**

Figure 9a shows the simulated spatial-temporal distribution of the isothermal liquid ( $q_{lh}$ ) and thermal liquid fluxes ( $q_{lT}$ ) for

0–100-cm soil depths. Before the rain, the gradient of soil-water matric potential and temperature was weak, but liquid water movement was enhanced with increasing soil-water matric potential after the rain. The pattern of the isothermal liquid flux  $q_{lh}$  was similar to that of the matric potential gradients; a zero flux occurred above 25 cm depth in the absence of rain on 18 July 2017. However, zero flux moved to 40 cm after a rainfall event on 24 July, and separated the soil profile into two different moisture zones. During the 7-day experimental period (18–24 July 2017), the maximum value of  $q_{lh}$  flux was close to  $0.02 \text{ cm h}^{-1}$  in the absence of rain on July 18th, increasing to  $0.12 \text{ cm h}^{-1}$  in the surface soil on 21 July due to an extreme rainfall event. The pattern of the  $q_{lT}$  flux with the zero flux plane was at approximately 50 cm, increasing to  $0.011 \text{ cm h}^{-1}$  during the rain period and by an order of magnitude in comparison to that before the rain. Moreover, the closed areas in the shallow layers at depths of 0–10 cm were triggered by the rainfall event, indicating that fluctuation in soil water was strongly related to the soil temperature gradient.

The zero-flux isothermal vapor flux was similar to that of the isothermal liquid flux (Fig. 9b). The flux remained

**Table 5** Calibrated hydraulic and thermal parameters for different soil depths used in the model

| Soil depth(cm) | Hydraulic parameters                    |   |      | Thermal parameters                |          |           |          |
|----------------|---|---|------|-----------------------------------|----------|-----------|----------|
|                | $\theta_f(\text{cm}^3 \text{ cm}^{-3})$ | $\theta_s(\text{cm}^3 \text{ cm}^{-3})$ | $n$  | $\alpha \text{ (cm}^{-1}\text{)}$ | $b_1$    | $b_2$     | $b_3$    |
| 5              | 0.01                                    | 0.27                                    | 1.62 | 0.055                             | 0.18E+17 | -0.16E+18 | 0.32E+18 |
| 15             | 0.03                                    | 0.26                                    | 1.41 | 0.044                             | 0.15E+17 | -0.17E+18 | 0.32E+18 |
| 25             | 0.002                                   | 0.36                                    | 1.65 | 0.016                             | 0.14E+17 | -0.16E+18 | 0.32E+18 |
| 40             | 0.004                                   | 0.21                                    | 1.53 | 0.006                             | 0.15E+17 | -0.16E+18 | 0.32E+18 |
| 60             | 0.008                                   | 0.29                                    | 1.63 | 0.008                             | 0.15E+17 | -0.16E+18 | 0.32E+18 |
| 100            | 0.009                                   | 0.31                                    | 1.61 | 0.008                             | 0.15E+17 | -0.16E+18 | 0.32E+18 |

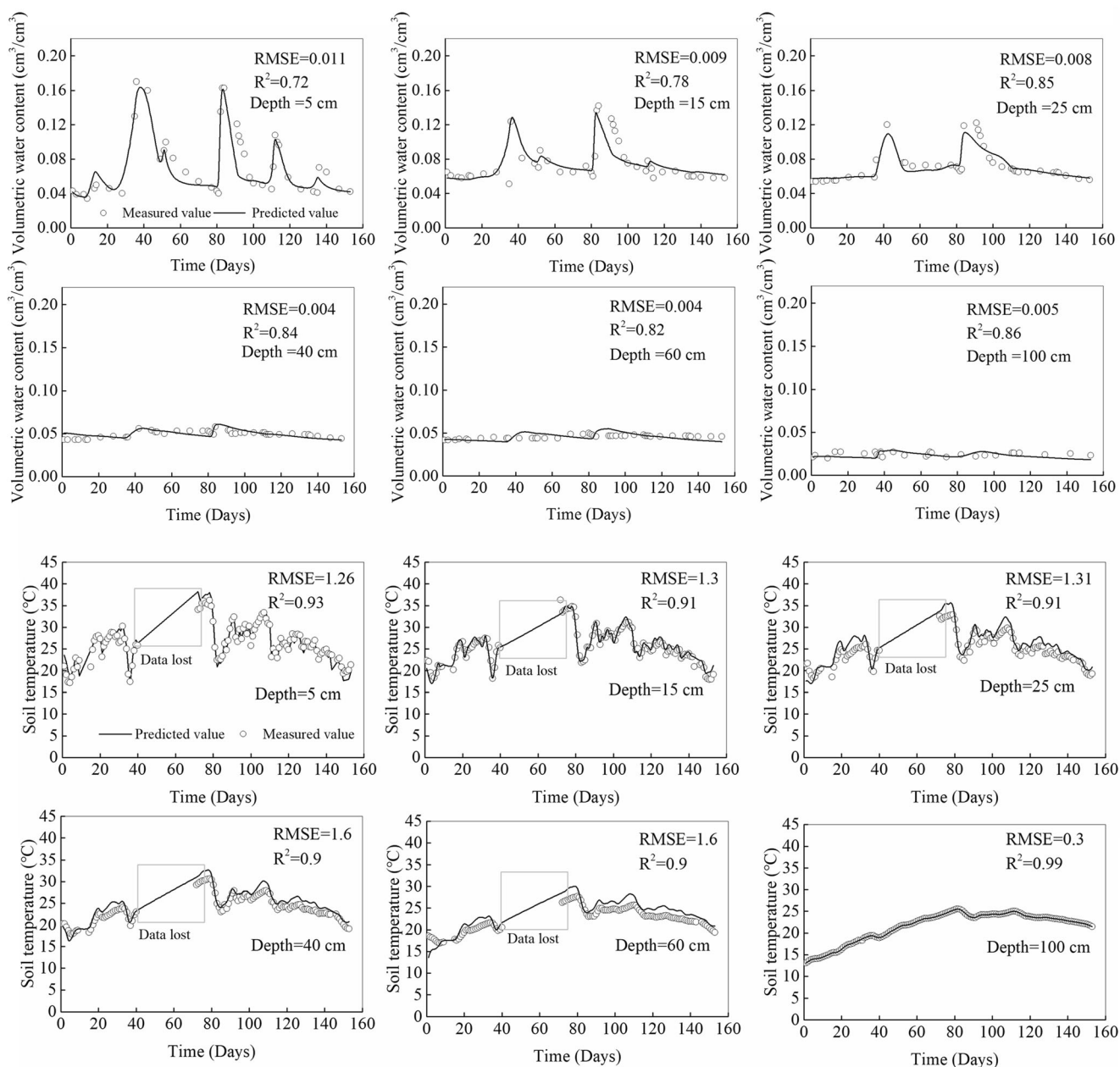


**Fig. 6** Measured versus simulated **a** soil-water content and **b** soil temperatures at different depths, used for calibration

fairly stable at depths of approximately 5 cm. The value of  $q_{vh}$  varied from  $5.4 \times 10^{-8}$  to  $0.002 \text{ cm h}^{-1}$  at the land surface. Furthermore, there was almost no  $q_{vh}$  flux below the zero-flux plane, especially after a rain event. Meanwhile, the spatial-temporal distribution of  $q_{vT}$  was similar to the distribution of  $q_{IT}$  during the study period. Above the zero-flux plane at the depth of 10 cm, the fluctuation in  $q_{vT}$  flux was notable, with  $q_{vT}$  rising to  $0.031 \text{ cm h}^{-1}$ ; however, below the lower zero flux plane, fluctuation in  $q_{vT}$  was very weak due to a dry soil layer with soil-water content close to the wilting point.

## The response of liquid and vapor movement in soil to rain

### Liquid and vapor transfer in the absence of rain

Figure 10a shows the spatio-temporal dynamics of  $q_{lh}$  in the soil profile from 0 to 100-cm depth on 18 July with no rainfall. During the study phase, in the time period from 01:00 to about 24:00,  $q_{lh}$  was strong at the surface layer and showed a maximum flux at the time of 13:00. Meanwhile, the  $q_{lh}$  flux, including both a positive value at 0–5 cm depth and a negative value at 10–

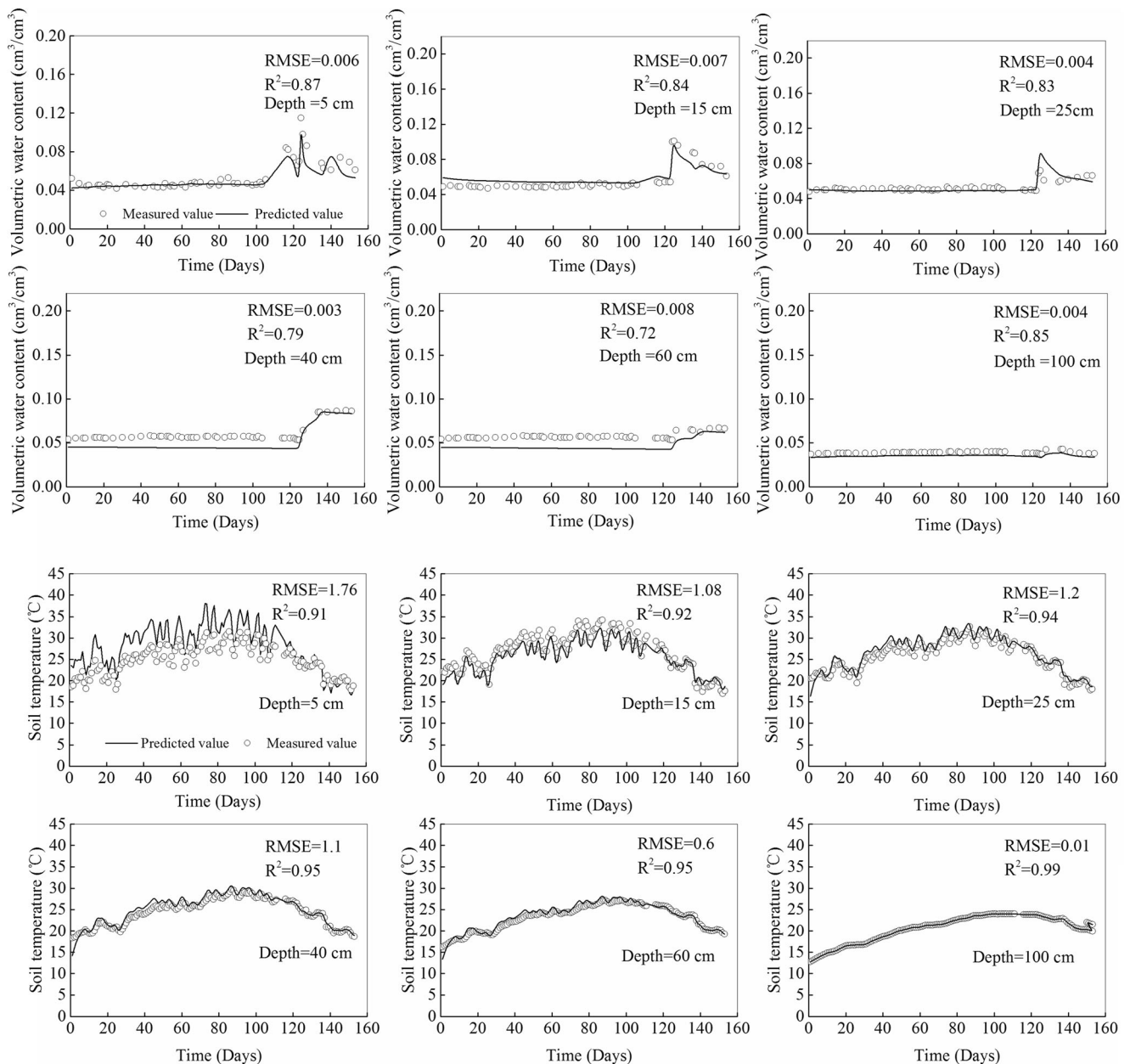


**Fig. 7** Measured versus simulated **a** soil-water content and **b** soil temperature at different depths used for model validation

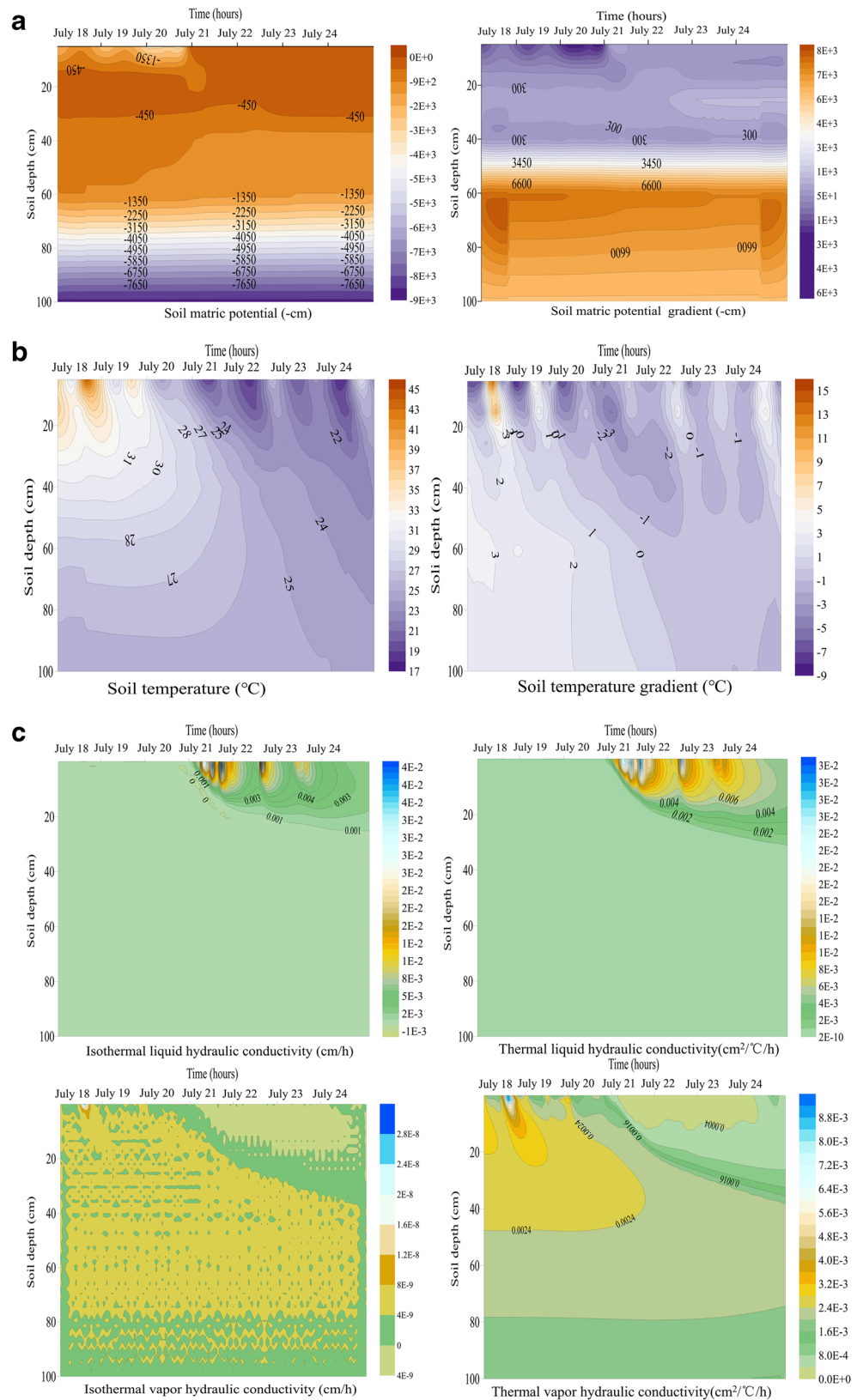
15 cm depth, indicated that  $q_{lh}$  included simultaneous upward and downward water flow. The movement of  $q_{IT}$  was downward to a maximum depth of 30 cm, but it was so low that it could be ignored compared with  $q_{lh}$  in the upper layer.

Figure 10b depicts the distribution of  $q_{vh}$  and  $q_{vT}$  in the soil profile. The value of  $q_{vh}$  was very low during the study phase. In contrast,  $q_{vT}$  became the major component of the total water flux in the dry soil.  $q_{vT}$  was positive from the soil surface to 30 cm depth. The value of  $q_{vT}$  at the land surface was very high after 09:00 reaching its maximum value of 0.06 cm h<sup>-1</sup> at 13:00.

Based on the space-time distribution of liquid water and water vapor fluxes, the transfer pattern of soil water was divided into three phases throughout the day: first

(before dawn, 01:00–07:00), second (daytime, 08:00–18:00) and last (midnight, 19:00–00:00; Fig. 10c). In the first phase, liquid water flux was the main water flux in the soil profile, forming a convergent plane at the depth of 10 cm due to the dual effect of soil matric potential gradient and temperature gradient. The  $q_{lh}$  moved to this plane, and  $q_{vT}$  was transported to the above, facilitating condensation of soil water. The transfer pattern of soil water was opposite in the second phase, in that the plane was divergent, possibly accelerating the loss of soil water. During the last phase, the soil-water transfer showed simultaneous divergent and convergent planes. The  $q_{lh}$  and  $q_{vT}$  were dominant fluxes at the depth of 5 cm, and

**Fig. 8** **a** Changes in soil matric potential and matrix potential gradient. **b** Changes in soil temperature and soil temperature gradient. **c** Changes in isothermal liquid hydraulic conductivity, thermal liquid hydraulic conductivity, isothermal vapor hydraulic conductivity, and thermal vapor hydraulic conductivity



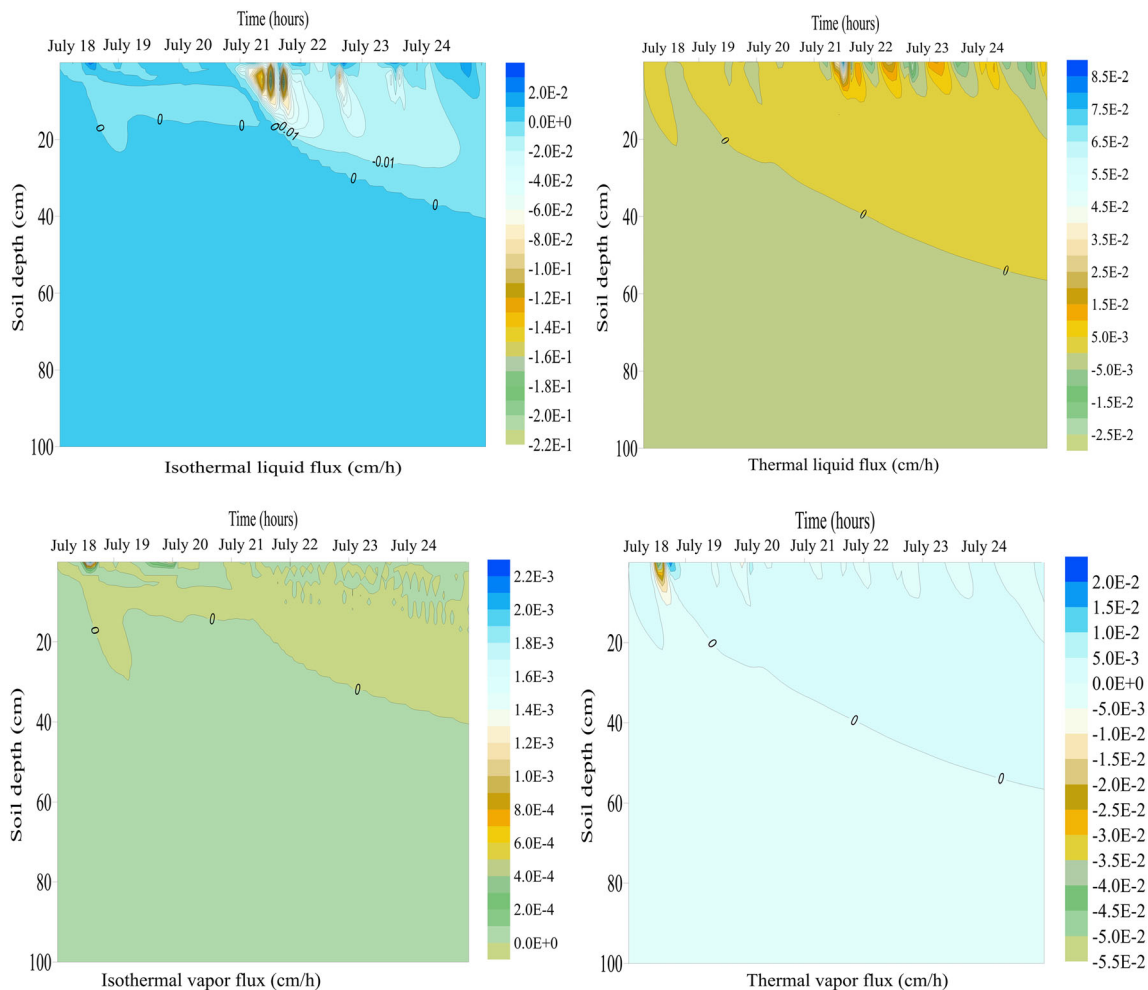


**Fig. 9** **a** Changes in isothermal and thermal liquid fluxes during the study period at 100-cm soil depth. **b** Changes in isothermal and thermal vapor fluxes during the study period at 100-cm soil depth

exhibited divergent planes. The  $q_{IT}$  was divergent at 10 cm and convergent at 30 cm, indicating soil-water evaporation from the top layer (10 cm) and condensation in the deeper layer (30 cm).

#### Liquid and vapor transfer during an extreme rainfall event

An extreme rainfall event occurred on 21 July from 01:00 to 11:00. Figure 11a shows the changes in the  $q_{lh}$  and  $q_{IT}$  fluxes along the soil profile on 21 July with rainfall. The matric potential at 0–20 cm depth was relatively high during the rain event. The direction of the flux during the three stages was downward across the entire soil profile, with a maximum value 2 h after the rain ended. However, the  $q_{IT}$  flux was very weak during the rainfall period and close to zero at nighttime after the rain.

Figure 11b shows that the  $q_{vh}$  and  $q_{vT}$  fluxes had low variability from the ground surface to 40 cm soil depth; the value of  $q_{vh}$  was close to zero for the three phases

because the matric potential had little or no effect on vapor transfer in the soil. Similarly, the  $q_{vT}$  flux in the dry vadose zone was inhibited by the rainfall event, compared to the vapor fluxes without rainfall.

Daytime was also divided into three phases including the daytime rain (01:00–11:00), daytime after the rain (12:00–18:00) and nighttime after the rain (19:00–24:00). Figure 11c shows the transfer pattern of soil water throughout the day during the rain. During rainfall, the transfer pattern of soil water was similar for the three phases;  $q_{lh}$  became the major component of all soil-water fluxes, and rainfall became redistributed to approximately 25 cm depth. In addition, although the  $q_{vT}$  transfer was relatively low, it could not be ignored because of its possible effect on water flux in two soil layers (5 and 40 cm). Two planes of zero-heat flux occurred in the soil profile: one was a convergent at 5-cm depth, where water condensation occurred; the other was a divergent at 40-cm depth, which could force soil water to deeper soil layers.

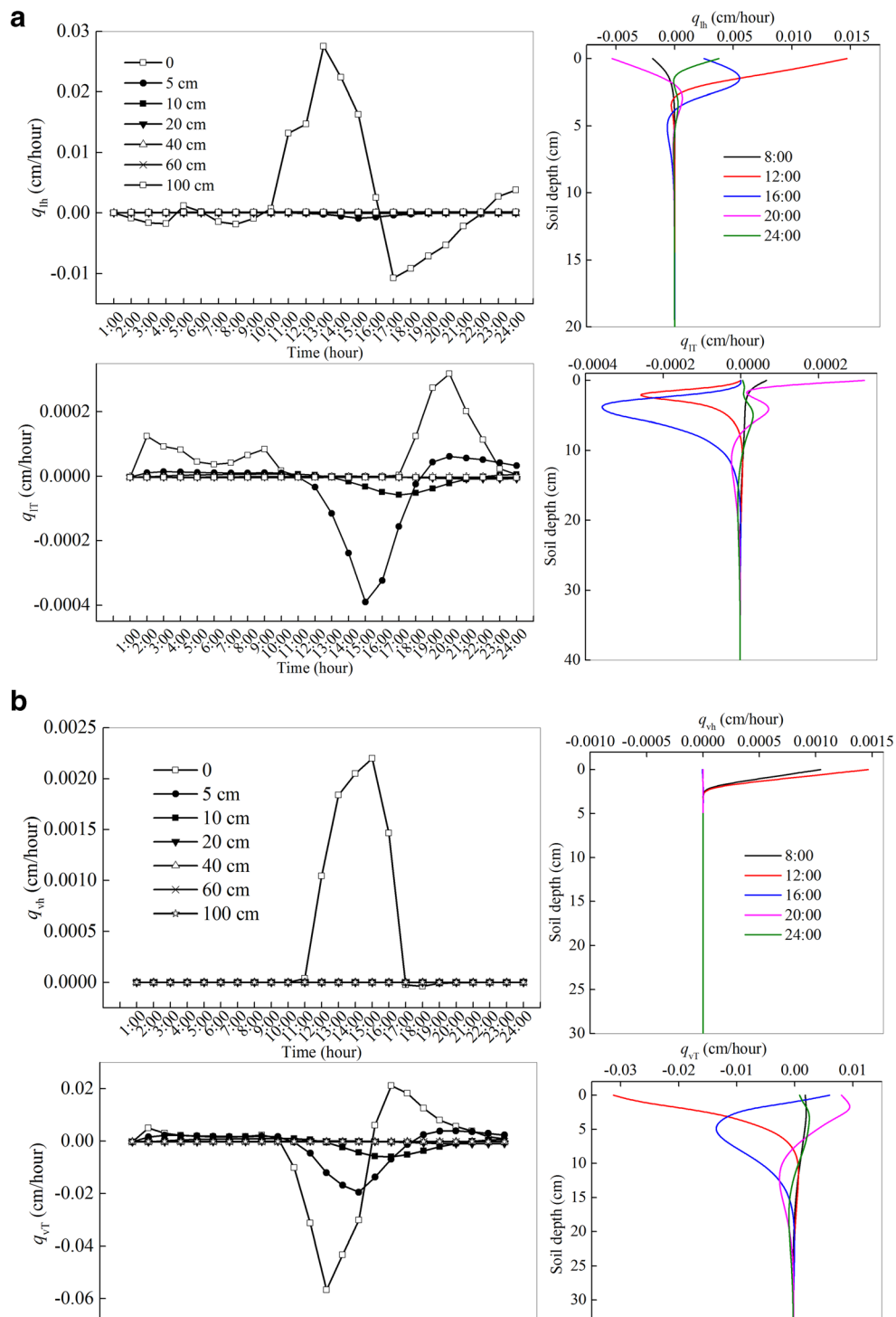


**Fig. 10 a** Spatio-temporal dynamics of isothermal liquid flux ( $q_{lh}$ ) and thermal liquid flux ( $q_{lT}$ ) before a rain event. **b** Spatio-temporal dynamics of isothermal vapor flux ( $q_{vh}$ ) and thermal vapor flux ( $q_{vT}$ ) before a rain

event. **c** Soil-water flux pattern in isothermal liquid flux ( $q_{lh}$ ), thermal liquid flux ( $q_{lT}$ ), isothermal vapor flux ( $q_{vh}$ ) and thermal vapor flux ( $q_{vT}$ ) 1 day before a rain event

### Liquid and vapor transfer after a rainfall event

Figure 12a,b shows the corresponding variability in the  $q_{lh}$  and  $q_{lT}$  fluxes in the soil profile at depths of 0–100 cm on 24 July, 2 days after an extreme rainfall event. The changes

in  $q_{lh}$  flux was still relatively strong at 0–40 cm depth, with positive  $q_{lh}$  flux at 0–10 cm, and negative below 10 cm. The  $q_{lT}$  flux was mostly negative in the soil profile and it was mainly affected at shallow depths; but it changed to positive during the nighttime (20:00–03:00).

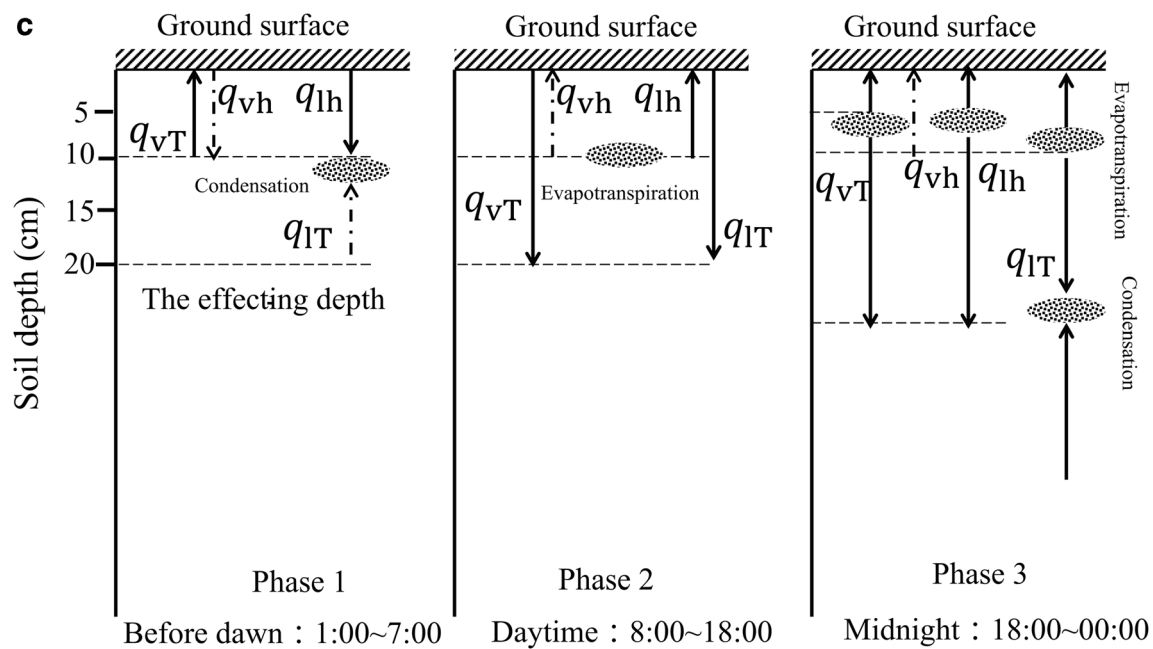


Fig. 10 (continued).

The  $q_{vh}$  flux was weak and the direction of the flux was downward across the entire soil profile during the three phases. The value of  $q_{vT}$  was moved to the soil surface driven by the temperature gradient during daytime, and the magnitude of the flux increased to  $0.004 \text{ cm h}^{-1}$  at 05:00. The  $q_{vT}$  flux was positive at 20–60 cm depth, and negative below 60 cm during the nighttime, indicating that water flowed in two directions.

Figure 12c shows the transfer pattern of soil water throughout the day after a rain period. The  $q_{lh}$  remained as the main water flux in the soil profile. A divergent plane formed at the depth of 10 cm, indicating that soil water was moved to the soil surface by evaporation, and migrated to a deeper (below 40 cm) layer in this plane. However, during the nighttime, two types of zero-heat flux planes occurred for the  $q_{vT}$  flux: one was a convergent plane at 10 cm depth, with soil-water condensation, and the other was a divergent plane at the depth of 40 cm, with soil-water movement up to the surface and downward to 60 cm. In the second phase, one of the convergent planes moved down to a depth of 20 cm. In addition, the  $q_{vT}$  flux was negative and appeared as a divergent plane at a depth of about 15 cm throughout the three phases, indicating that soil water moved downward above this plane.

### Distribution of root biomass

To understand how soil-water fluxes in shallow soil layers can be used by desert plants, typical desert shrubs *H. ammodendron*, *Calligonum mongolicum*, and *N. sphaerocarpa* were selected, and the root biomass

distribution was investigated. The distribution of root biomass differed significantly with the profile depth. Root biomass was low in deep soil layers of below 80–200 cm; most roots were concentrated at depths 0–60 cm, with about 30% being 5-year-old *H. ammodendron* roots, 60% being 10-year-old *H. ammodendron* roots, 76% being *N. sphaerocarpa* roots, and 72% being *C. mongolicum* roots (Fig. 13).

## Discussion

### Composition of soil-water fluxes throughout the day

Vapor movement is often an important part of the total water flux in the vadose zone in regions with scarce rainfall (Saito et al. 2006). This study showed that thermal vapor flux ( $q_{vT}$ ) was very important in soil-water transfer at the surface of sandy soils with no rainfall, accounting for 99% of the total soil-water flux in daytime. This study confirmed the results of Du et al. (2017), who found that the thermal vapor flux comprised almost total water flux in the desert vadose zone, and occurred in the upper layer only during a prolonged drought period. In addition, in the case of an extreme rainfall event, the isothermal liquid flux ( $q_{lh}$ ) increased steadily and became dominant due to rainfall infiltration and the contribution of  $q_{lh}$  to the total water flux at 0–20 cm depth. Thus, other fluxes could be ignored, which is because the capillary connections of the soil pores were very strong, leading to a dramatic reduction in vapor flux in shallow soil layers (Sakai et al. 2009). During rainfall, the matric potential gradients in the upper soil

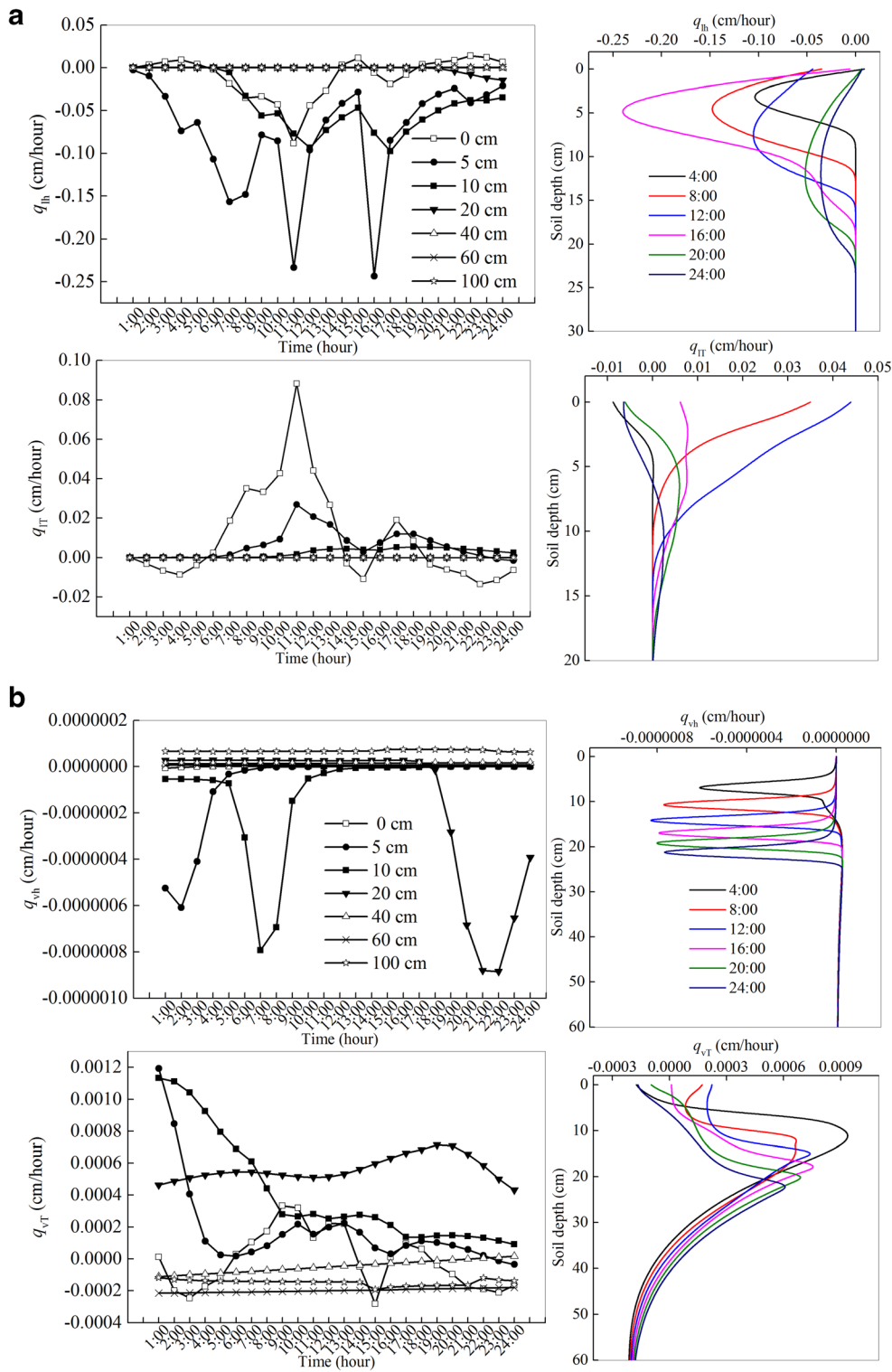


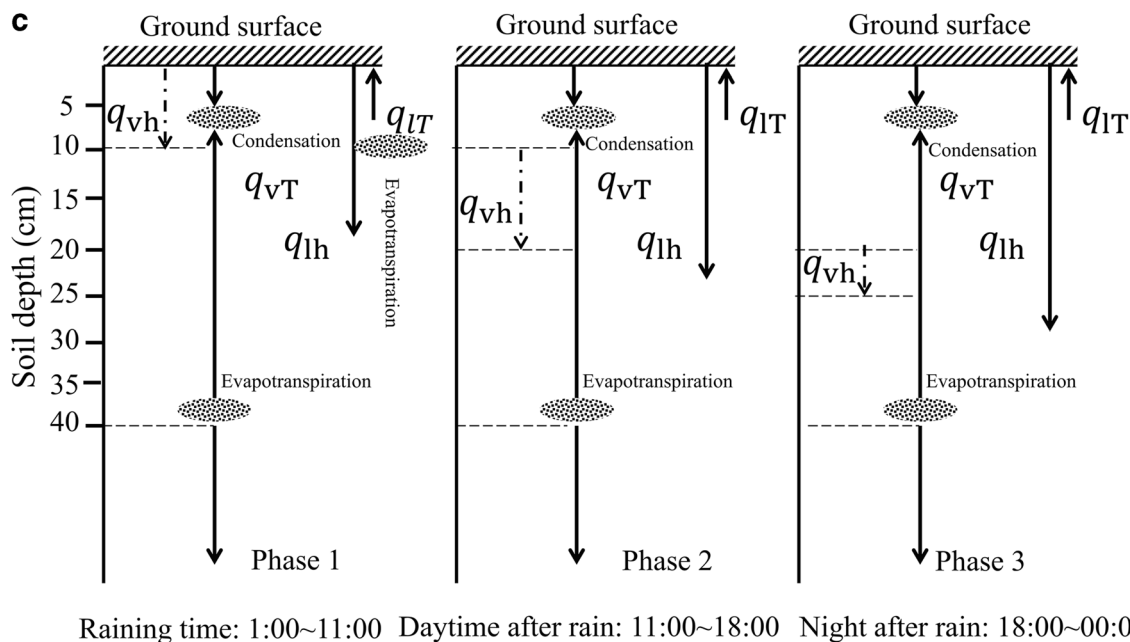
**Fig. 11 a** Spatio-temporal dynamics of isothermal liquid flux ( $q_{lh}$ ) and thermal liquid flux ( $q_{lr}$ ) during a rain event. **b** Spatio-temporal dynamics of isothermal vapor flux ( $q_{vh}$ ) and thermal vapor flux ( $q_{vr}$ ) during a rain

event. **c** Soil-water flux pattern in isothermal liquid flux ( $q_{lh}$ ), thermal liquid flux ( $q_{lr}$ ), isothermal vapor flux ( $q_{vh}$ ) and thermal vapor flux ( $q_{vr}$ ) during a rain event

layers were very large, while the soil temperature gradients were weak. After a rainfall event, soil-water redistribution processes continued, the isothermal liquid flux ( $q_{lh}$ ) remained

as the main water flux at the depth of 0–20 cm, but the direction changed to upward. However, thermal liquid flux ( $q_{lr}$ ) and thermal vapor flux ( $q_{vr}$ ) increased during this period, with





Raining time: 1:00~11:00 Daytime after rain: 11:00~18:00 Night after rain: 18:00~00:00

Fig. 11 (continued).

the  $q_{IT}$  accounting for 29.4% of the total flux in daytime; the simulated results showed that the  $q_{vT}$  was approximately 11.8% of the total water fluxes. Deb et al. (2011) also found that the value of  $q_{vT}$  accounted for 10.4% of the total flux in the unsaturated soils in semiarid and arid regions of New Mexico, USA. Cahill and Parlange (1998) examined water transfer in the Mojave Desert after an irrigation event, and found that the contribution of  $q_{vT}$  to total moisture flux ranged from 10 to 30%. Therefore, during the soil drying process (no rainfall), soil-water fluxes eventually transformed to vapor fluxes along the soil profile as a result of dry sandy soil and steep temperature gradients, particularly for shallow soils of desert sand dune systems.

Earlier studies have shown that water-limited environments are usually dominated by bare sandy soils with an extremely dry soil layer in which soil moisture is dominantly in vapor phase with a large capillary suction head (Goss and Madliger 2007; Mahdavi et al. 2021). However, the pattern of soil-water fluxes in a desert soil can vary due to different rainfall scenarios; with normal rainfall events (4–6 mm/day), the thermal vapor flux (from the soil temperature gradient) comprised almost the total water flux in the desert vadose zone and occurred only in the upper layer; meanwhile, the thermal liquid flux approached 0 and could be ignored with respect to the total water flux of the dry soil (Du et al. 2017). However, a thermal liquid flux had a large effect on the water flux after an extremely large rainfall event in this study. In addition, the thermal vapor flux reached 30-cm soil depth in this study during a rainfall event, but it was affected by 20 cm only with a 7-mm/day rainfall event (Zeng et al. 2009). Rainfall prevented or weakened the vapor flux movement in the desert

vadose zone, and these effects may be more significant with an increase in the amount of rainfall.

### The relationship between soil-water transfer and utilization by plants

Although arid desert areas have low rainfall, the short-term enrichment of water supply with rainfall events plays an important role in plant growth (Schwinning and Sala 2004). Distribution characteristics of plant root systems are critical for obtaining soil water (Xu et al. 2011). It was found that during long drought periods, the  $q_{vT}$  and  $q_{IT}$  fluxes converged at nighttime at 5 and 30 cm depth, indicating that soil water increased through condensation (Fig. 10c), and this probably provided moisture for plant root uptake. Wang (2015) found that soil-water vaporization often occurs at some depth below (5–30 cm) the ground surface, and pore vapor needs to be transported by an upward positive heat gradient through the upper dry soils into the ambient atmosphere. Zhang et al. (2016) defined this phenomenon as a second type of a canopy effect, where significant moisture accumulation occurred due to vapor transfer. In addition, after a rainfall event, the  $q_{IT}$  and  $q_{vT}$  fluxes moved down in the soil profile and the affected depth increased, especially for the  $q_{vT}$  which moved to below 60 cm (Fig. 11c); this suggested that soil-water variability between depths of 60 and 100 cm may be affected or that water may be recharged. Zhou et al. (2016) found that 60% of water for 5-year-old *H. ammodendron* came from soil depth from surface to 50 cm, while 58.3% of water for *N. sphaerocarpa* originated in deep soil (below 100 cm) in low rainfall conditions. Others found that vapor transport with

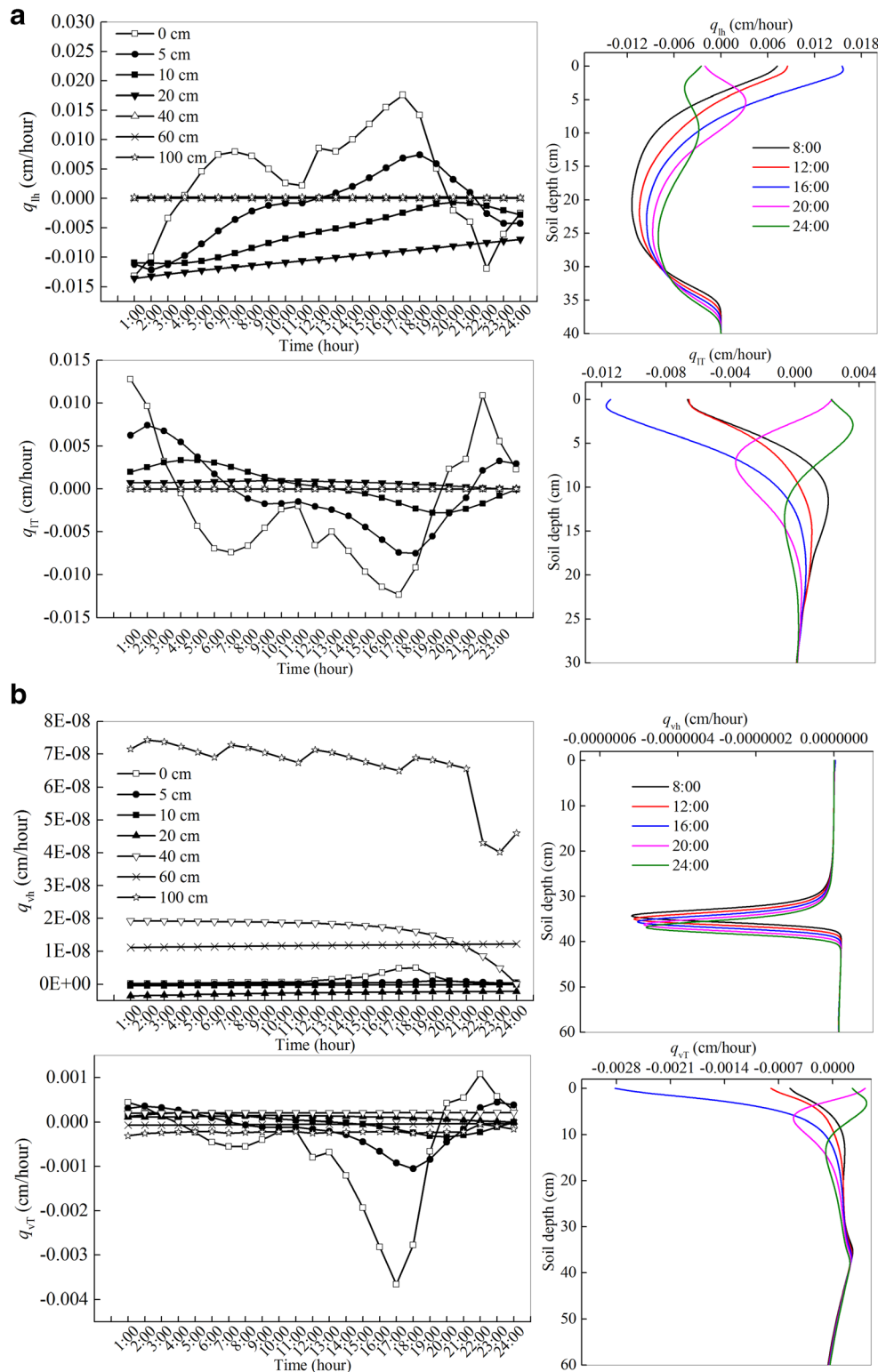


**Fig. 12 a** Spatio-temporal dynamics of isothermal liquid flux ( $q_{1h}$ ) and thermal liquid flux ( $q_{1T}$ ) after a rain event. **b** Spatio-temporal dynamics of isothermal vapor flux ( $q_{vh}$ ) and thermal vapor flux ( $q_{vT}$ ) after a rain event.

**c** Soil-water flux pattern in isothermal liquid flux ( $q_{1h}$ ), thermal liquid flux ( $q_{1T}$ ), isothermal vapor flux ( $q_{vh}$ ) and thermal vapor flux ( $q_{vT}$ ) 1 day after a rain event

convergence at land surface may result in small daily variability in water contents (Bittelli et al. 2008; Huang et al. 2015), and soil-water vapor adsorption may also supply water to

vegetation in seasons with a severe water deficit (Ramírez et al. 2007). In particular, thermally driven vapor flow and condensation supplemented moisture to plant roots in dry

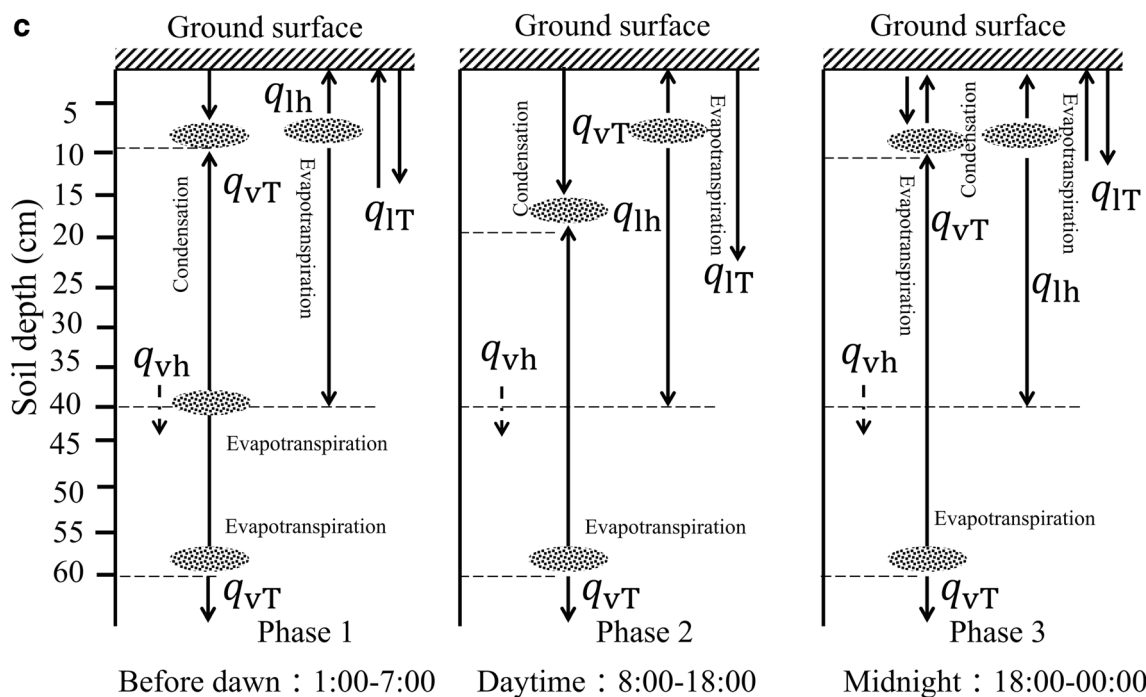


Fig. 12 (continued).

climates in the northern Mojave Desert (Garcia et al. 2011). Ehleringer et al. (1991) found that desert annual plants and succulent perennials exhibited a complete dependence on soil water in desert environments.

### Conclusions

Investigating soil-water infiltration and recharge dynamics from rainfall in sand dune ecosystems is a key issue in the

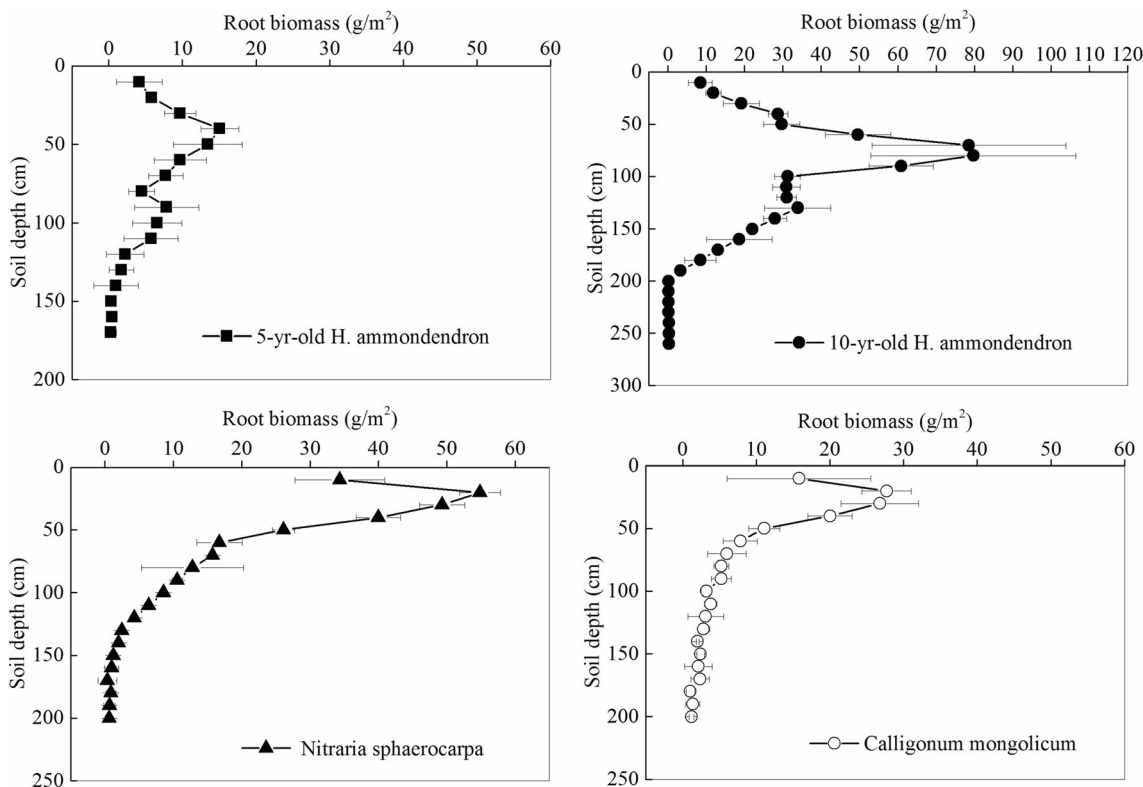


Fig. 13 Vertical distribution of root systems: *Haloxylon ammodendron* at 5 and 10 years of age, *Calligonum mongolicum*, and *Nitraria sphaerocarpa*

ability to study the effects of soil–plant–atmosphere interactions on shallow water movement in areas where water resources are scarce. Many challenges were conducted to distinguish and quantify water fluxes directly. Simulation methods provide a good understanding of soil-water movement that controls the shallow-soil moisture regime in desert environments, and they are augmented by field data. Therefore, first, in-situ field experiments were conducted to determine the effects of the soil matric potential and soil temperature on soil water and water transport pattern in the vadose zone, and, second, the Hydrus-1D model was used to accurately simulate 1D soil-water dynamics for different soil-water scenarios based on the coupled soil mass and energy budget.

The results showed that thermally driven vapor flow was the dominant component of the total water flux at the surface of dry soil; water flux frequently switched between condensation at night and evaporation in daytime. This may constitute a potential pathway of dew formation; however, during extreme rainfall periods, isothermal liquid flux between soil depths of 0 and 30 cm, and near-surface thermally driven liquid flow comprised nearly all of the total water flux. Although thermal vapor flow was restricted to the shallow soil layers, its flux was strong in the lower layers (depths of approximately 40–100 cm). In addition, when water infiltration ceased after rainfall, isothermal liquid flux was gradually replaced by thermally driven liquid and vapor flow, in particular, thermally driven vapor flow continued to increase as drought continued, and became the major source of increase in water content in these soils. This process significantly affected the soil-water balance, plant water use, and ecohydrological relations in this desert environment.

Taken together, the results showed that an extreme rainfall event, especially when coinciding with clustered light rainfall events, can infiltrate into deep soil layers with the help of soil matric potential gradient in dry sandy soil. Water near the soil surface and deeper soil moisture is governed primarily by longer-duration soil vapor patterns, and soil vapor is the most available form of water in the soil after a long drought. In particular, movement of water vapor caused by a soil temperature gradient drives the surface soil-water balance after an extreme rainfall event in a desert environment with a large day-and-night temperature difference. These results increase the understanding of the mechanisms of rainfall infiltration in desert soil, and may aid in efforts to revegetate desertified environments.

**Funding information** This work was jointly financed by key project of the National Natural Science Foundation of China (No. 41630861), and the National Science Foundation for Young Scientists of China (No. 41501577).

**Data availability statement** The data that support the findings of this study are available on request from the corresponding author. Data are not publicly available due to privacy or ethical restrictions.

## Declarations

**Conflict of interest statement to the manuscript** No conflict of interest exists in the submission of this article.

## References

- Andraski BJ, Stonestrom DA, Michel RL, Halford KJ, Radyk JC (2005) Plant-based plume-scale mapping of tritium contamination in desert soils. *Vadose Zone J* 4(3):819–827
- Arnone E, Pumo D, Viola F, Noto LV (2013) Rainfall statistics changes in Sicily. *Hydrol Earth Syst Sci* 17(7):2449–2458
- Aronica G, Cannarozzo M, Noto LV (2002) Investigating the changes in extreme rainfall series recorded in an urbanised area. *Water Sci Technol* 45(2):49–54
- Bittelli M, Ventura F, Campbell GS, Snyder RL, Gallegati F, Pisa PR (2008) Coupling of heat, water vapor, and liquid water fluxes to compute evaporation in bare soils. *J Hydrol* 362(3–4):191–205
- Bouyoucos GJ (1915) Effect of temperature on movement of water vapor and capillary moisture in soils. *J Agric Res* 5:141–172
- Bristow KL, Horton R (1996) Modeling the impact of partial surface mulch on soil heat and water flow. *Theor Appl Climatol* 54(1):85–98
- Cahill AT, Parlange MB (1998) On water vapor transport in field soils. *Water Resour Res* 34(4):731–739
- Cass A, Campbell GS, Jones TL (1984) Enhancement of thermal water vapor diffusion in soil. *Soil Sci Soc Am J* 48(1):25
- Chen M, Willgoose GR, Saco PM (2014) Spatial prediction of temporal soil moisture dynamics using Hydrus-1D. *Hydrol Process* 28(2):171–185
- Chung SO, Horton R (1987) Soil heat and water flow with a partial surface mulch. *Water Resour Res* 23(12):2175–2186
- Deb SK, Shukla MK, Sharma P, Mexal JG (2011) Coupled liquid water, water vapor, and heat transport simulations in an unsaturated zone of a sandy loam field. *Soil Sci* 176(8):387–398
- Du CY, Yu JJ, Wang P, Zhang YC (2017) Analysing the mechanisms of soil water and vapour transport in the desert vadose zone of the extremely arid region of northern China. *J Hydrol* 558:592–606
- Ehleringer JR, Phillips SL, Schuster W, Sandquist DR (1991) Differential utilization of summer rains by desert plants. *Oecologia* 88(3):430–434
- Garcia CA, Andraski BJ, Stonestrom DA, Cooper CA, Wheatcraft SW (2011) Interacting vegetative and thermal contributions to water movement in desert soil. *Vadose Zone J* 10(3):1117
- Goss K, Madliger M (2007) Estimation of water transport based on in situ measurements of relative humidity and temperature in a dry Tanzanian soil. *Water Resour Res* 43:W05433
- Huang JT, Hou RZ, Yang HB (2015) Diurnal pattern of liquid water and water vapor movement affected by rainfall in a desert soil with a high water table. *Environ Earth Sci* 75(1):1–16
- Knapp AK, Claus B, Briske DD, Classen AT, Luo Y, Markus R, Smith MD, Smith SD, Bell JE, Fay PA (2008) Consequences of more extreme precipitation regimes for terrestrial ecosystems. *Bioscience* 58(9):811–821
- Li HS, Wang WF, Zhan HT, Qiu F, An LZ (2010) New judgement on the source of soil water in extremely dry zone. *Acta Ecol Sin* 30(1):1–7
- Madi R, Rooij G (2015) Numerical and Experimental Quantification of coupled water and water vapor fluxes in very dry soils. EGU General Assembly Conference, EGU, Munich, Germany
- Mahdavi SM, Fujimaki H, Neyshabouri MR (2021) On water vapor movement and evaporation in a sandy soil column. *Eurasian Soil Sci* 54:249–256

- Marsily GD (1986) Quantitative hydrogeology: ground-water hydrology for engineers. Academic, San Diego
- McVicar TR, Roderick ML, Donohuea RJ, Li LT, Van Niel TG, Thomas A, Grieser J, Jhajharia D, Himri Y, Mahowald NM, Mescherskaya AV, Kruger AC, Rehman S, Dinpashohl Y (2012) Global review and synthesis of trends in observed terrestrial near-surface wind speeds: implications for evaporation. *J Hydrol* 416(1):182–205
- Milly PCD (1982) Moisture and heat transport in hysteretic, inhomogeneous porous media: a matrix head-based formulation and a numerical model. *Water Resour Res* 18(3):489–498
- Milly PCD (1984) A linear analysis of thermal effects on evaporation from soil. *Water Resour Res* 20(8):1075–1085
- Milly PCD (1996) Effects of thermal vapor diffusion on seasonal dynamics of water in the unsaturated zone. *Water Resour Res* 32(3):509–518
- Mualem, Yechezkel (1976) A new model for predicting the hydraulic conductivity of unsaturated porous media. *Water Resour Res* 12(3):513–522
- Nassar IN, Horton R (1997) Heat, water, and solution transfer in unsaturated porous media: I, theory development and transport coefficient evaluation. *Transp Porous Media* 27(1):17–38
- Nassar IN, Horton R, Globus AM (1992) Simultaneous transfer of heat, water, and solute in porous media: II. experiment and analysis. *Soil Sci Soc Am J* 56(5):1357–1365
- Noy-Meir I (1973) Desert ecosystems: environment and producers. *Annu Rev Ecol Syst* 4(1):25–51
- Parlange MB, Cahill AT, Nielsen DR, Hopmans JW, Wendroth O (1998) Review of heat and water movement in field soils. *Soil Tillage Res* 47(1):5–10
- Penman HL (1940) Gas and vapor movements in the soil: the diffusion of vapors through porous solids. *J Agric Sci* 30(3):437–462
- Philip JR (1957) Evaporation, and moisture and heat fields in the soil. *J Atmos Sci* 14(4):354–366
- Philip JR, Vries DAD (1957) Moisture movement in porous materials under temperature gradients. *Eos Trans Am Geophys Union* 38(2):222–232
- Ramírez DA, Bellot J, Domingo F, Blasco A (2007) Can water responses in *Stipa tenacissima* L. during the summer season be promoted by non-rainfall water gains in soil? *Plant Soil* 291(1):67–79
- Richards LA (1931) Capillary conduction of liquids in soil through porous media. *Physics* 1(5):318–333
- Saito H, Imnek J, Mohanty BP (2006) Numerical analysis of coupled water, vapor, and heat transport in the vadose zone. *Vadose Zone J* 5(2):784
- Sakai M, Toride N, Simunek J (2009) Water and vapor movement with condensation and evaporation in a sandy column. *Soil Sci Soc Am J* 73(3):707
- Scanlon BR (1994) Water and heat fluxes in desert soils: 1. field studies. *Water Resour Res* 30(3):721–734
- Scanlon BR, Keese K, Reedy RC, Simunek J, Andraski BJ (2003) Variations in flow and transport in thick desert vadose zones in response to paleoclimatic forcing (0–90 kyr): field measurements, modeling, and uncertainties. *Water Resour Res* 39(7):303
- Schwinning S, Sala OE (2004) Hierarchy of responses to resource pulses in arid and semi-arid ecosystems. *Oecologia* 141(2):211–220
- Ucles O, Villagarcía L, Cantón Y, Lazaro R, Domingo F (2015) Non-rainfall water inputs are controlled by aspect in a semiarid ecosystem. *J Arid Environ* 113:43–50
- Uclés O, Villagarcía L, Cantón Y, Domingo F (2016) Partitioning of non rainfall water input regulated by soil cover type. *Catena* 139:265–270
- UN (2021) World map. <https://www.un.org/Depts/Cartographic/map/profile/world.pdf>. Accessed June 2021
- van Genuchten TM (1980) A closed-form equation for predicting the hydraulic conductivity of unsaturated soils. *Soil Sci Soc Am J* 44(5):892–898
- Webb SW, Ho CK (1998) Review of enhanced vapor diffusion in porous media. <https://www.osti.gov/servlets/purl/656582>. Accessed June 2021
- Westra S, Fowler HJ, Evans JP, Alexander LV, Roberts NM (2015) Future changes to the intensity and frequency of short-duration extreme rainfall: future intensity of sub-daily rainfall. *Rev Geophys* 52(3):522–555
- Willmott CJ (1981) On the validation of models. *Phys Geogr* 2(2):184–194
- Wu YJ, Du TS, Ding RS, Yuan YS, Li S, Tong L (2017) An isotope method to quantify soil evaporation and evaluate water vapor movement under plastic film mulch. *Agric Water Manag* 184:59–66
- Wang X (2015) Vapor flow resistance of dry soil layer to soil water evaporation in arid environment: an overview. *Water* 7(8):4552–4574
- Xu Q, Li HB, Chen JQ, Cheng XL, Liu SR, An SQ (2011) Water use patterns of three species in subalpine forest, Southwest China: the deuterium isotope approach. *Ecohydrology* 4(2):236–244
- Yao YY, Tian Y, Charles A, Li X, Zheng Y, Zheng CM (2018a) Role of groundwater in the dryland Ecohydrological system: a case study of the Heihe River basin. *J Geophys Res: Atmos* 123:6760–6776
- Yao YY, Zhang CM, Tian Y, Li X, Liu J (2018b) Eco-hydrological effects associated with environmental flow management: a case study from the arid desert region of China. *Ecohydrology* 11(1):e1914
- Zeng YJ, Su Z, Wan L, Yang Z, Zhang T, Tian H, Shi X, Wang XL, Cao W (2009) Diurnal pattern of the drying front in desert and its application for determining the effective infiltration. *Hydrol Earth Syst Sci* 13(6):703
- Zeng YJ, Su B, Wan L, Wen J (2011) Numerical analysis of air-water-heat flow in unsaturated soil: is it necessary to consider airflow in land surface models? *J Geophys Res* 116(20):20107
- Zhang ZY, Wang WK, Yeh TJ, Chen L, Wang ZF, Duan L, An K, Gong CC (2016) Finite analytic method based on mixed-form richards' equation for simulating water flow in vadose zone. *J Hydrol* 537:146–156
- Zhang Q, Wei GA (2003) Analysis of inverse humidity respiration process of surface soil in desert near oasis. *J Desert Res* 34(4):379–384
- Zhang J, Zhang YM, Zhou ZB, Nan WU, Wang HL, Chen RY (2007) Study on daily change of soil moisture content under the effect of microbiotic crusts in the Gurbantonggut Desert, Xinjiang, China. *Arid Zone Res* 24(5):661–668
- Zhang YY, Zhao WZ, Fu L (2017) Soil macropore characteristics following conversion of native desert soils to irrigated croplands in a desert-oasis ecotone, Northwest China. *Soil Tillage Res* 168:176–186
- Zhao LW, Zhao WZ (2014) Water balance and migration for maize in an oasis farmland of Northwest China. *Chin Sci Bull* 59(34):4829–4837
- Zhao LJ, Li Y, Xiao HL, Cheng GD, Zhou MX, Yang YG, Li CZ, Jian Z (2011) Isotopic evidence for the moisture origin and composition of surface runoff in the headwaters of the Heihe River basin. *Chin Sci Bull* 56(1):406–415
- Zhou H, Zhao WZ, Yang QY (2016) Root biomass distribution of planted *Haloxylon ammodendron* in a duplex soil in an oasis: desert boundary area. *Ecol Res* 31(5):673–681
- Zhuang YL, Zhao WZ (2017) Dew formation and its variation in *Haloxylon ammodendron* plantations at the edge of a desert oasis, northwestern China. *Agric For Meteorol* 247:541–550